Title
Novel Heat Removal Enhancement and Reduction Methods and Optimized Surface Treatments for Several Engineering Applications

Author
Haghighi, Arman

Publication Date
2018

Peer reviewed|Thesis/dissertation

UNIVERSITY OF CALIFORNIA
RIVERSIDE

Novel Heat Removal Enhancement and Reduction Methods and Optimized Surface Treatments for Several Engineering Applications

A Dissertation submitted in partial satisfaction
of the requirements for the degree of

Doctor of Philosophy

in

Mechanical Engineering

by

Arman Haghighi

March 2018

Dissertation Committee:
Dr. Kambiz Vagai, Chairperson
Dr. Cengiz Ozkan
Dr. Masaru Rao

The Dissertation of Arman Haghighi is approved:

Committee Chairperson

University of California, Riverside

ABSTRACT OF THE DISSERTATION

Novel Heat Removal Enhancement and Reduction Methods and Optimized Surface Treatments for Several Engineering Applications

by

Arman Haghighi

Doctor of Philosophy, Graduate Program in Mechanical Engineering
University of California, Riverside, March 2018
Dr. Kambiz Vafai, Chairperson

Metallic foams have increasingly gained attention due to their superior structural, acoustic, mixing and filtering characteristics. To further enhance the thermal features of these materials, a single or an array of metallic porous structures of various geometries are introduced on the inside surface of the partially heated wall of a channel with laminar flow. The challenge is to enhance the forced convection heat transfer rate from the heated wall to the working fluid while minimizing the pressure drop penalty caused by implementing these structures. Forced convective heat transfer rate from the heated wall to the fluid, as well as the average pressure drop along the channel are numerically studied with respect to the case with no structural extensions.

Various Aluminum metallic foams with different structural parameter values of Porosity (ε), Pore diameter (d_p^*), Darcy number (Da) are studied for the most common working fluids used in practical applications. Accordingly, the optimum geometrical

conditions of the system is extensively explored considering geometrical parameters such as block's height, width and spacing between them. Our results demonstrate that the optimum conditions yield considerable *Nu* enhancement ratios compared to the case of a channel with no metallic structural foam mounted inside. As such, thermal performance of metal foams can be substantially enhanced for heat removal in applications for solar collectors, compact heat exchangers, electronic cooling, etc. for only a modest increase in the pressure drop.

The second part of this thesis, addresses the issue of natural convection in cavities which is widely found in cooling electronics devices, heat exchangers, solar thermal collectors, heating and ventilating applications and energy conservation in refrigeration units. Implementations of the insulating features in a cavity is a solution for the goal of reduction in the overall heat transfer through the cavity. Therefore, heat transfer reduction capabilities of a vertical or a horizontal adiabatic partial partition fixed in a differentially heated cavity with insulated top and bottom walls are analyzed and compared. The effects of length and location of the partition is taken into account for aspect ratios from 1 to 4 and for Rayleigh numbers from 10^3 to 10^6. Different characteristics of square and higher aspect ratio cavities are compared and a comprehensive correlation of the heat transfer reduction is introduced, incorporating all the pertinent parameters. Furthermore, the optimized configurations and features for insulating purposes are established and discussed. Based on our results, vertical baffles more efficiently reduce heat transfer, in most cases.

Table of contents:

List of tables (abbreviated):

List of figures (abbreviated):

CHAPTER 1: Heat removal enhancement in a channel with a single or an array of metallic foam obstacles

Nomenclature:

AR aspect ratio, [$AR = H / R$]

c_p specific heat, [$J / kg.K$]

D distance between Blocks, [m]

D^* non-dimensional distance between blocks

Da Darcy Number

d_f fiber diameter, [m]

d_p mean pore diameter, [m]

d_p^* non-dimensional mean pore diameter

F Forchheimer coefficient

G shape function

g gravitational acceleration, [m / s^2]

H height of block, [m]

H^* non-dimensional height of block

h local heat transfer coefficient, [$W / m^2.K$]

K permeability, [m^2]

k thermal conductivity, [$W / m.K$]

k_r conductivity ratio of metal to fluid

L	length of channel, [m]
L_e	length of from the heated section to exit, [m]
L_h	length of heated portion of the wall, [m]
L_i	length from inlet to the heated section, [m]
Nu	local Nusselt number
$\overline{Nu}$	average Nusselt number
$\overline{Nu_o}$	average Nusselt number in the absence of blocks
n	number of blocks
Pr	Prandtl number
P	non-dimensional pressure
P_o	non-dimensional pressure in the absence of blocks
p	local pressure, [N/m^2]
q''	heat flux, [W/m^2]
R	channel height, [m]
R_c	ratio of effective porous conductivity to fluid conductivity
Re	Reynolds number
T	local temperature, [K]
T_o	temperature at the inlet [K]
u, v	dimensionless velocity components, [m/s]
u^*, v^*	local velocity components

u_o average velocity at the inlet, $[m/s]$

W width of block, $[m]$

W^* non-dimensional width of block

x, y Cartesian coordinates

x^*, y^* non-dimensional Cartesian coordinates

Greek symbols:

θ non-dimensional temperature

ρ fluid density, $[kg/m^3]$

ε porosity

μ dynamic viscosity $[Pa.s]$

ψ dimensionless stream function

Subscripts:

e channel exit

eff effective

f fluid

h heated

i channel inlet

s solid

w wall

1. Introduction

Forced convective heat transfer inside a channel with a heated wall, is a classical problem which has been studied extensively. Some works have sought to enhance the performance in this important configuration by means of modifying the geometry of the channel or the thermal characteristics of the fluid [1-4]. Wang et al [1] explored effects of using a wavy channel instead of a straight walled channel. Albojamal et al. [2] increased the thermal conductivity of the fluid by implementing nano-particles and modifying the geometry of the walls to wavy shaped ones at the same time. Chabane [3] considered using horizontal baffles in the channel in order to enhance the performance of a heat collector.

To further enhance the heat removal or absorbing rates for forced convective heat transfer in a channel, is based on implementation of porous medium within different configurations. Thermal efficiency of such systems has received a great deal of attention due to the need to keep up with the demand for compact heat exchangers [5-8]. The goal is to adjust the flow and exploit the superior heat transfer capabilities of metal foam by taking advantage of the large active surface area between the solid and the fluid phases compared to the regular tube or channel case. Lee and vafai [5] obtained an exact solution considering Local thermal Non Equilibrium (LTNE) to analytically attain the temperature profiles, Nu number and the temperature difference between the solid and fluid phases in a channel fully filled with a porous medium. Koh and Colony [7] analyzed the effectiveness of using a porous medium in a cooling passage. Kaviany [8] considered a steady laminar flow through a porous channel bounded by two isothermal parallel plates and analytically studied the involved convective heat transfer through transport equations based on the quadratic-extended Darcy flow model.

Some works have focused on a single or an array of porous blocks in a channel [9-11]. Huang and Vafai [9] numerically investigated the problem of steady forced convection in a parallel plate channel with isothermal walls and an array of mounted porous blocks. Based on their results the array of porous blocks considerably decreases the heat removal rate from the flat plate. Fu et al. [10] studied thermal performance of a single porous obstacle in a laminar channel flow, considering all the non-Darcian effects. Their numerical work demonstrated enhanced effectiveness of high porosity blocks. Chick et al. [11] numerically investigated forced convection on the inner heated wall of a channel with intermittent heated porous blocks, to improve the thermal performance.

Metallic porous medium foams have gained attention over the past several decades, due to their superior structural, acoustic, mixing and filtering characteristics. Recently the thermal features of this new technology has increasingly been investigated as well. Comprehensive reviews on the subject have been carried out by Banhart and Zhao [12,13]. Also Mahjoob and Vafai [14] have provided a comprehensive review of different fluid and thermal transport models for metallic foams. In addition to enhanced surface area, the high thermal conductivity of these material enables their implementation in a wide variety of technologies such as heat pipes, thermal insulation, combustors, compact heat sinks in electronic devices, compact heat exchangers, and solar thermal collectors [15-19]. Kim et al. [15] studied thermal performance of forced convective air-cooling of aluminum-foam heat sinks in electronics. Their experimental work reveals that the metal foam heat sinks are up to 28% more thermally effective compared to the plate fin heat sinks. Boomsma et al. [17] experimentally investigated metal foams for forced convective cooling in compact heat exchangers. They reported that thermal resistance of metal foams compact heat exchanger is two to three times lower as compared to other commercially available heat exchangers. Angirasa [18] considered a channel fully filled with metallic fibrous foam and reported the forced convection numerical results, which showed that a substantial thermal performance increase is caused by using a porous substrate. Mahajan [19] studied the finned metal foam heat sinks for electronic cooling. In their work the distance between fin heat sinks was filled with metal foams, and reported heat transfer enhancement factors up to 2 compared to the case without the metal foam fillings.

The aim of the current study is to effectively implement metal as partial obstruction in a channel to enhance the heat transfer rate. A comprehensive investigation of the flow field and the pressure drop along with the heat transfer enhancement capabilities of metallic foam partial obstructions placed on the heated section of the wall is presented. The previous works with partial metallic foam fillings have mostly considered a single fixed length for the heated section of the wall, with a specific Prandtl Number for the fluid (either water or air). Also, in the previous works a thorough study of the pressure drop penalty caused by using a metallic porous medium was not accomplished

In the current work, Aluminum is utilized as the building material of the mounted porous slabs, due to ubiquity of Aluminum based open-cell metal foams in industry. The structural characteristics of the porous domain are retrieved from earlier well established, experimental works. Furthermore our investigation concurrently covers both thermal and flow alterations caused by the metal foams for all the considered cases. Results for both water and air as the working fluid are presented and compared, for three common rectangular, elliptic and triangular shaped metal foam obstructions.

2. Problem definition and assumptions

A schematic drawing of the horizontal parallel-plate channel partially heated from below, single or array of blocks mounted on the lower plate and the pertinent boundary conditions are depicted in Figure 1.1. Channel width is represented by *R*. Parameters *x* and *y* are dimensional distances in the two coordinate systems directions from lowest point in at the channel entrance. In this figure u_0 is the average value of the parabolic fully developed velocity profile at the entrance and T_0 is the uniform temperature at the entrance. Parameters *H*, *W* represent height and width of the barriers in both cases, and *D* denotes the distance between them in the array format.

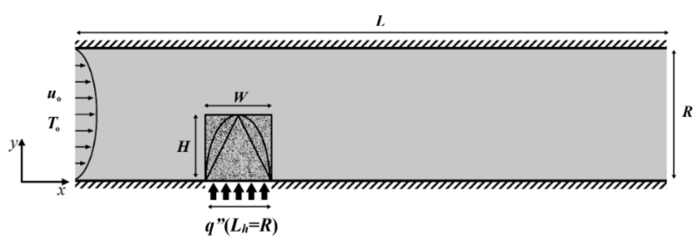

(a)

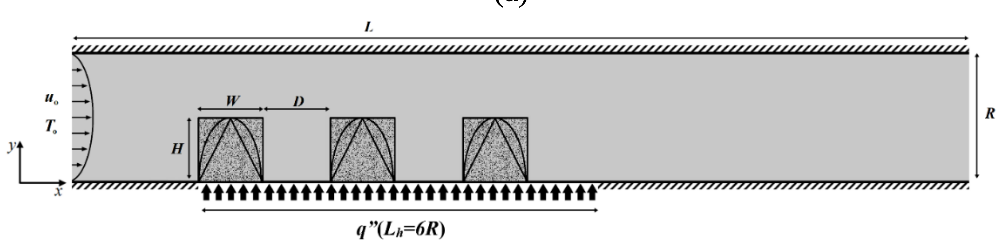

(b)

Figure 1.1 Schematic of the channel studied in the present work, along with representative triangular, rectangular and elliptic porous Aluminum blocks. (a) Single block setting (b) Multiple blocks setting.

In Figure 1.1a the constant heat flux (q'') is applied right below the block with a width equal to the height of the channel. In Figure 1.1b the length of the heated region with constant heat flux (q'') is considered equal to 6*R*. Total length of the physical domain in Figure 1.1a and Figure 1.1b are L= 9R and L=14R respectively. The single block, or the first block for multiple blocks case, is mounted at a distant L_i = 2R from the inlet. In both cases the remaining walls are insulated and the flow exits the physical domain at a length L_e=6R after the heated region. An extended computational domain is considered downstream of the physical domain which is long enough to ensure fully developed conditions at the channel exit. This would assure conditions downstream of the considered physical domain exit plane does not impact the hydrodynamic conditions inside the domain.

3. Governing equations and boundary conditions

The fluid and the solid matrix are considered isotropic and homogeneous with constant thermophysical properties. Moreover the porous structure is considered to be non-deformable, while the flow is considered laminar, incompressible, inviscid and steady. The problem is considered two dimensional with negligible effect of gravity. Also for energy considerations, viscous dissipation, work done by pressure and radiation effects are considered negligible. Governing equations in the clear fluid region are:

Conservation of Mass (Continuity Equation):

$$\nabla.\left(\vec{\mathrm{v}}\right)=0 \tag{1.1}$$

Momentum Equation (Navier-Stokes):

$$\rho\left(\vec{\mathrm{v}}.\nabla\vec{\mathrm{v}}\right) = -\nabla p + \mu\nabla^2\vec{\mathrm{v}} \tag{1.2}$$

Energy Equation:

$$\rho c_p\left(\vec{\mathrm{v}}.\nabla T\right) = k_f\nabla^2 T \tag{1.3}$$

In these equations $\vec{\mathrm{v}}$ is the local velocity in the domain, while T and p are local pressure and temperatures, respectively. Parameters ρ, μ, c_p and k_f are fluid density, dynamic viscosity, specific heat capacity and thermal conductivity of the fluid. For simplification, the angle brackets representing volume-averaged variables will be omitted in equations related to the porous domain, for example u in the porous region is equivalent to $\langle u \rangle$. The flow through the metal foam is considered to be single phase and local thermodynamic equilibrium (LTE) is considered between the fluid and the solid. As such the governing equations in the Porous region are:

Conservation of Mass (Continuity Equation):

$$\nabla.\left(\vec{\mathrm{v}}\right) = 0 \tag{1.4}$$

Momentum equation is based on the generalized Eq.(1.2) to incorporate the effects of inertia as well as friction caused by macroscopic shear in the porous domain [20,21]:

$$\frac{\rho}{\varepsilon^2}\left(\vec{\mathrm{v}}.\nabla\vec{\mathrm{v}}\right) = -\nabla p + \frac{\mu}{\varepsilon\rho}\nabla^2\vec{\mathrm{v}} - \frac{\mu}{k_f}\vec{\mathrm{v}} - \frac{\rho F\varepsilon}{K^{1/2}}\left|\vec{\mathrm{v}}\right|\vec{\mathrm{v}}\text{, where } \left|\vec{v}\right| = \sqrt{u^2 + v^2} \tag{1.5}$$

Energy Equation:

$$\rho c_p\left(\vec{\mathrm{v}}.\nabla T\right) = k_{eff}\nabla^2 T\text{, where: } k_{eff} = \varepsilon k_f + 1 - \varepsilon\ k_s \tag{1.6}$$

In these equations ε, K and F, are the porosity, permeability and Forchheimer coefficient of the porous structure. Also parameters k_{eff} and k_s represent the effective thermal conductivity and thermal conductivity of the solid material in the porous domain. These governing equations can be normalized by defining the following dimensionless parameters:

$$x^* \equiv \frac{x}{R},\ y^* \equiv \frac{y}{R},\ \overrightarrow{\mathrm{v}^*} \equiv \frac{\vec{\mathrm{v}}}{u_0}\ \left(u^* \equiv \frac{u}{u_0},\ \mathrm{v}^* \equiv \frac{\mathrm{v}}{u_0}\right),\ \theta \equiv \frac{T - T_0}{q'' R / k_f},\ P = \frac{p}{\rho u_0^2}$$

$$Re \equiv \frac{\rho_f u_0 R}{\mu_f},\ Da \equiv \frac{K}{R^2},\ k_r = \frac{k_s}{k_f},\ Pr \equiv \frac{\mu_f c_p}{k_f} \tag{1.7}$$

Amongst these variables, Reynolds number (Re) and Prandtl number (Pr) characterize the working fluid and the flow field, while Darcy number (Da) and Ratio of conductivities (k_r) identify the metal foam and its thermal features. The normalized governing equations in the fluid and porous domains can be combined into a single set, by considering ε and k_r equal to unity and Da as infinity for the fluid domain.

Continuity:

$$\nabla.\left(\overrightarrow{\mathrm{v}^*}\right) = 0 \tag{1.8}$$

Momentum:

$$\frac{1}{\varepsilon^2}\left(\overrightarrow{\mathrm{v}^*}.\nabla\overrightarrow{\mathrm{v}^*}\right) = -\nabla P + \frac{1}{\varepsilon Re}\nabla^2\overrightarrow{\mathrm{v}^*} - \frac{1}{ReDa}\overrightarrow{\mathrm{v}^*} - \frac{F\varepsilon}{\sqrt{Da}}\left|\overrightarrow{\mathrm{v}^*}\right|\overrightarrow{\mathrm{v}^*} \tag{1.9}$$

Energy:

$$\left(\overrightarrow{\mathrm{v}^*}.\nabla\theta\right) = \frac{R_c}{RePr}\nabla^2\theta = \frac{\varepsilon + (1-\varepsilon)K_r}{RePr}\nabla^2\theta \tag{1.10}$$

where R_c is the Ratio of Conductivities of the porous domain and the fluid, $R_c = k_{eff} / k_f$. Flow boundary conditions are comprised of no slip conditions on the top and bottom walls, while maintaining fully developed flow conditions at the inlet and the outlet.

Top and bottom plates: $u^* = \mathrm{v}^* = 0$

Entrance at $x^* = 0$: $u^* = 6y^*(1-y^*),\ \mathrm{v}^* = 0$ (1.11)

Exit at $x^* = L/R$: $\dfrac{\partial u^*}{\partial x^*} = 0, \mathrm{v}^* = 0$

Thermal boundary conditions are comprised of constant temperature at the inlet, fully developed conditions at the outlet and adiabatic conditions on the top and bottom walls except for the heated region with constant heat flux.

Top and bottom plates except the heated section: $\partial\theta/\partial y^* = 0$

Heated section: $$\partial\theta/\partial y^* = \begin{cases} -\dfrac{1}{R_c} & \text{adjacent to blocks} \\ 1 & \text{adjacent to fluid} \end{cases} \quad (1.12)$$

Entrance at $x^* = 0$: $\theta = 0$

Exit at $x^* = L/R$: $\partial\theta/\partial x^* = 0$

At the interface between the fluid and the porous domains continuity conditions are applied for the velocity field, normal and shear stresses, temperature and heat flux as described by the following equations: (Vafai and Kim [22], Sathe et al. [23])

Flow Interface Conditions:

$$u_p^*\big|_{s(x^*,y^*)} = u_f^*\big|_{s(x^*,y^*)}, \quad \mathrm{v}_p^*\big|_{s(x^*,y^*)} = \mathrm{v}_f^*\big|_{s(x^*,y^*)}, \quad P_p\big|_{s(x^*,y^*)} = P_f\big|_{s(x^*,y^*)}$$

$$\mu_{eff}\left.\frac{\partial \mathrm{v}_p^*}{\partial n}\right|_{s(x^*,y^*)} = \mu_f \left.\frac{\partial \mathrm{v}_f^*}{\partial n}\right|_{s(x^*,y^*)} \tag{1.13}$$

$$\mu_{eff}\left.\left(\frac{\partial u_p^*}{\partial n} + \frac{\partial \mathrm{v}_p^*}{\partial t}\right)\right|_{s(x^*,y^*)} = \mu_f \left.\left(\frac{\partial u_f^*}{\partial n} + \frac{\partial \mathrm{v}_f^*}{\partial t}\right)\right|_{s(x^*,y^*)}$$

Thermal Interface Conditions:

$$\theta_p\big|_{s(x^*,y^*)} = \theta_f\big|_{s(x^*,y^*)}$$

$$k_{eff}\left.\frac{\partial \theta_p}{\partial y}\right|_{s(x^*,y^*)} = k_f \left.\frac{\partial \theta_f}{\partial y}\right|_{s(x^*,y^*)} \tag{1.14}$$

where $s(x^*, y^*)$ is the contour representing the interface between the fluid and the porous domains, and *n* and *t* are directions normal and tangential with respect to this curve at any given point on it.

4. Numerical solution

The aforementioned governing partial differential equations and boundary conditions, were solved using COMSOL Multiphysics. The fluid flow, temperature and the heat flux at the interface between the porous and fluid, were coupled using the multiphysics module. And the finite element method (FEM) was utilized to directly solve the large sparse linear system of equations, with less than 10^{-4} relative error. For the cases of single block the dimensionless Geometrical Parameters are as follows:

$$AR \equiv \frac{H}{R},\ W^* \equiv \frac{W}{R} \tag{1.15}$$

where W^* is set to unity to cover the whole heated region of the wall. For the cases of multiple blocks the dimensionless Geometrical Parameters are as follows:

$$AR \equiv \frac{H}{R},\ W^* \equiv \frac{W}{R}, D^* \equiv \frac{D}{R}, n \equiv \text{number of blocks} \tag{1.16}$$

Pertaining input parameters in the governing equation are *Re*, ε, *Da*, *F*, *Pr* and k_r. Water and air are used as the working fluid in the channel with respective Prandtl values of *Pr*=0.7 and *Pr*=7. It is clear that utilizing metals with higher thermal conductivities would yield higher heat removal rates through the energy equation. In this study we consider Aluminum as the state of the art material for building metallic foams [24]. Therefore the conductivity ratio for Air (*Pr*=0.7) and water (*Pr*=7) in the channel are k_r=8200 and k_r=342 respectively. Values of *K* and *F* in the momentum equation can be evaluted based on other characteristics of the mettalic foam, such as Porosity, Average Pore Diameter (d_p) and average fiber diameter (d_f), through the equations introduced by Calmidi [6,7].

$$F = 0.00212(1-\varepsilon)^{-0.132}\left(\frac{d_f}{d_p}\right)^{-1.63} \tag{1.17}$$

$$\frac{K}{d_p^2} = 0.00073(1-\varepsilon)^{-0.224}\left(\frac{d_f}{d_p}\right)^{-1.11} \tag{1.18}$$

Where $d_f\,/d_p$ is also given as a function of the porosity:

$$\frac{d_f}{d_p} = 1.18\sqrt{\frac{(1-\varepsilon)}{3\pi}}\frac{1}{G} \tag{1.19}$$

Where G is the shape function and modifies the originally dodecahedron oriented expressions for an open cell foam:

$$G = 1 - e^{-(1-\varepsilon)/0.04} \tag{1.20}$$

In this work we study porosities: ε=0.75, 0.85, and 0.95 which covers common ranges of porosity for metallic foams. Therefore different values of d_p=1, 5 and 10*mm*, can be normalized based on the geometrical specifications of Calmidi's experimental work [25, 26]. In the performed experiments they considered the height of the channel equal to 50*mm*, therefore we can acquire d_p*=0.02, 0.1 and 0.2. Further, K and F can be calculated by means of above equations and finally K can also be normalized to obtain values of Da. As such the calculated properties of the Aluminum porous metallic material used for the purpose of this study are shown in Table 1.1. The bold formatted columns in the table represent non-dimensional values of ε and d_p^* as input parameters in our study and also their corresponding values for Da and F.

Table 1.1 Properties of Aluminum foam for different porosities and pore diameters, based on the work of Calmidi [23]

d_p (mm)	ε	d_f (mm)	K (m^2)	d_p*	d_f*	Da	F
1	**0.75**	0.1924	6.21×10^{-9}	**0.02**	3.85×10^{-3}	**2.48×10^{-6}**	**0.0374**
1	**0.85**	0.1506	9.13×10^{-9}	**0.02**	3.01×10^{-3}	**3.65×10^{-6}**	**0.0596**
1	**0.95**	0.1018	1.80×10^{-8}	**0.02**	2.04×10^{-3}	**7.22×10^{-6}**	**0.1306**
5	**0.75**	0.9618	1.55×10^{-7}	**0.1**	1.92×10^{-2}	**6.21×10^{-5}**	**0.0374**
5	**0.85**	0.7532	2.28×10^{-7}	**0.1**	1.51×10^{-2}	**9.13×10^{-5}**	**0.0596**
5	**0.95**	0.5088	4.51×10^{-7}	**0.1**	1.02×10^{-2}	**1.80×10^{-4}**	**0.1306**
10	**0.75**	1.9237	6.21×10^{-7}	**0.2**	3.85×10^{-2}	**2.48×10^{-4}**	**0.0374**
10	**0.85**	1.5065	9.13×10^{-7}	**0.2**	3.01×10^{-2}	**3.65×10^{-4}**	**0.0596**
10	**0.95**	1.0175	1.80×10^{-6}	**0.2**	2.04×10^{-2}	**7.22×10^{-4}**	**0.1306**

Our simulations produce the velocity, pressure and temperature fields, which can be used to introduce meaningful parameters to study the heat removal capacity of the setting along with the required pumping power. Local Nusselt number at any point on the heated part of the wall and the average Nusselt number along this heated region can be calculated based on non-dimensional temperature as follows:

$$Nu = \frac{hd}{k_f} = \frac{q''(R/k_f)}{T_w - T_m} = \frac{1}{\theta_w - \theta_m} \tag{1.21}$$

$$\overline{Nu} \equiv \int_{x=L_i}^{x=L_i+L_h} Nu\ dx \Bigg|_{y=R} = \int_{x=L_i/R}^{x=(L_i+L_h)/R} Nu\ dx \Bigg|_{y^*=1} \tag{1.22}$$

where h is the local heat transfer coefficient. Average Nu provides a measure of the total heat removal rate from the heated portion of the wall. Nusselt number enhancement ratio is defined as follows and it represents heat removal adjustments caused by introducing the barriers inside the channel compared to the situation of the same channel without the blocks,

$$\frac{\overline{Nu}}{\overline{Nu_o}} = \frac{\overline{Nu} \text{ in the presence of the barriers}}{\overline{Nu} \text{ in the absence of the barriers}} \tag{1.23}$$

Since we intend to simultaneously study heat enhancement along with pressure drop, introducing a similar quantity to compare the pressure reduction along the channel is needed. Average pressure drop and pressure drop augmentation ratio can be introduced as:

$$\Delta\overline{P} = \int_{entrance} \frac{P}{\rho u_0^2} - \int_{exit} \frac{P}{\rho u_0^2} \tag{1.24}$$

$$\frac{\Delta\overline{P}}{\Delta\overline{P_o}} = \frac{\Delta\overline{P} \text{ in the presence of the barriers}}{\Delta\overline{P} \text{ in the absence of the barriers}} \tag{1.25}$$

Average pressure drop ($\Delta\overline{P}$) represents the difference between the average pressure at the inlet and the physical domain's exit plane. Consequently, pressure drop augmentation ratio compares this value for cases of the channel with and without the barriers. It should be mentioned that in the absence of body forces applying the blocks on the lower or the upper walls would create completely symmetrical geometries and boundary conditions and therefore similar symmetrical flow and temperature fields and would yield same values of Nusselt and Pressure drop. Therefore subsequent collected results can be extended for the cases of blocks on the upper plate if required by the application.

5. Grid independence and validation

The triangular mesh used in this work has a non-uniform distributed grid size. The mesh is further dense inside the blocks and in areas at a close vicinity of the porous structures as well as the channel walls compared to other regions. This would ensure capture of the interfacial and boundary conditions as well as precise flow and thermal fields in this area. The size of the mesh is controlled through four independent parameters which are maximum and minimum element size, maximum growth rate and curvature resolution.

To check grid independence, three different mesh types with different sizes were created, the first one being the coarsest and the third one being the finest. The difference between the average Nu resulting from each of these meshes types are less than 0.5%. Moreover the difference between the results of mesh 2 and mesh 3 are less than 0.1% apart. The average *Nu* results for four different specific random cases of a single block mounted in the channel were gathered, utilizing these mesh types. These results are presented and compared in Figure 1.2 as a sample of the grid independence. These cases include situations with water or air, as well as different geometrical features of the metallic structure. Mesh three is mainly composed of elements with maximum and minimum size of 2.8×10^{-2} and 4×10^{-4} respectively. Maximum element growth rate is 1.1 and curvature factor equals 0.25. Near the boundaries these parameters are chosen to create an even finer mesh. As an example for the case of a single triangular block half of the height of the channel, the computational domain is discretized to roughly 7×10^{4} domain elements and 2×10^{3} boundary triangular elements. The insignificant difference between the results from mesh 3 and the less packed versions, constitutes great accuracy for this mesh size and hence it will used for all the subsequent simulations in this work.

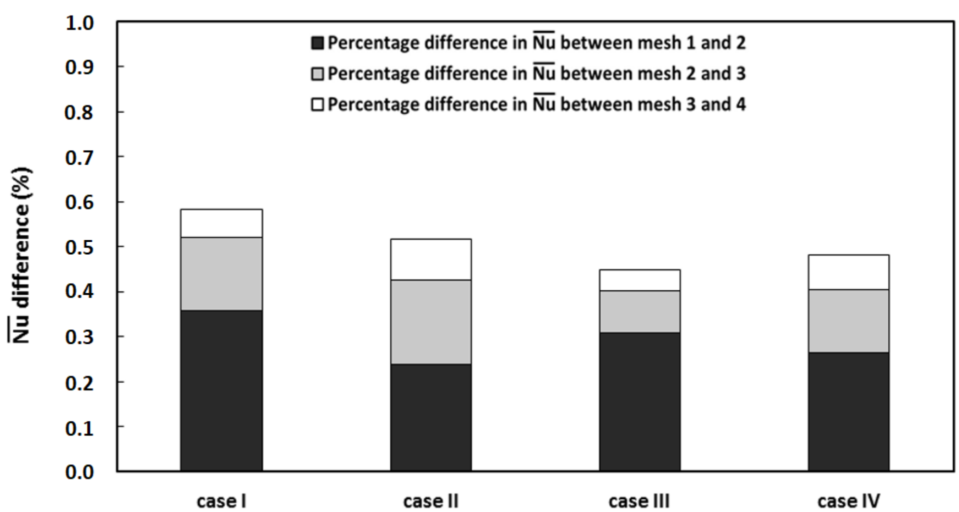

Figure 1.2 Effect of mesh concentration and grid independence study, for
Case I) Triangular block, *Pr*= 7, k_r=342, *Re*=1000, ε=0.75, d_p^*=0.1, *AR*=0.25
Case II) Rectangular block, *Pr*= 7, k_r=342, *Re*=1500, ε=0.85, d_p^*=0.02, *AR*=0.5
Case III) Triangular block, *Pr*= 0.7, k_r=8200, *Re*=1000, ε=0.95, d_p^*=0.1, *AR*=0.5
Case IV) Elliptic block, *Pr*= 0.7, k_r=8200, *Re*=1500, ε=0.85, d_p^*=0.2, *AR*=0.25

To check grid independence, three different mesh types with different sizes were created, the first one being the coarsest and the third one being the finest. The difference between the average Nu resulting from each of these meshes types are less than 0.5%. Moreover the difference between the results of mesh 2 and mesh 3 are less than 0.1% apart. The average *Nu* results for four different specific random cases of a single block mounted in the channel were gathered, utilizing these mesh types. These results are presented and compared in Figure 1.2 as a sample of the grid independence. These cases include situations with water or air, as well as different geometrical features of the metallic structure. Mesh three is mainly composed of elements with maximum and minimum size of 2.8×10^{-2} and 4×10^{-4} respectively. Maximum element growth rate is 1.1 and curvature factor equals 0.25. Near the boundaries these parameters are chosen to create an even finer mesh. As an example for the case of a single triangular block half of the height of the channel, the computational domain is discretized to roughly 7×10^{4} domain elements and 2×10^{3} boundary triangular elements. The insignificant difference between the results from mesh 3 and the less packed versions, constitutes great accuracy for this mesh size and hence it will used for all the subsequent simulations in this work.

To validate our model, we compared results from our simulations to other similar works in the published literature for flow and heat transfer in a channel with mounted solid or porous blocks. Figure 1.3 illustrate comparisons with the work of Young and Vafai [27] regarding a channel with multiple solid blocks mounted on the inside of the lower plate at *Re*=800. The blocks have conductivities ten times that of the fluid and are heated right below them by a surface heat flux while other walls are adiabatic. The blocks are a quarter of the height of the channel both in height and width and their distance are a quarter of the height of the channel as well. Same geometrical and physical specifications were used to produce the streamlines and isotherms utilizing our model. Additionally, Figure 1.4 presents the comparison of the local Nusselt number on the surface of these blocks from our solution and Young and Vafai's results.

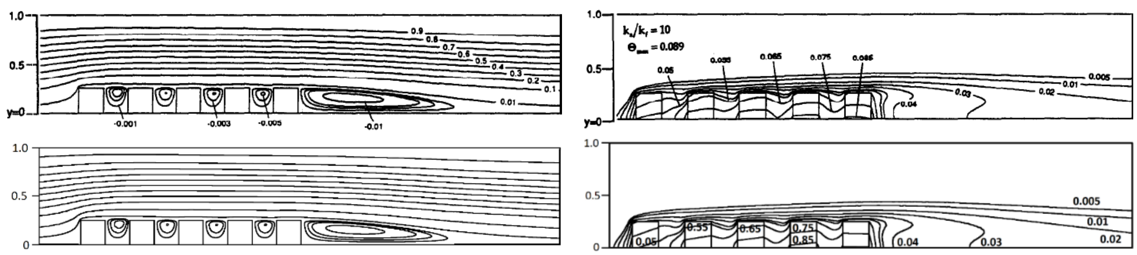

(a) (b)

Figure 1.3 Flow in a parallel plate channel for the base line heat flux case: k_s/k_f=10 and Re=800. Results from Young and Vafai [25] located on top, and present work located on the bottom, (a) Streamlines (ψ : -0.001, -0.003, -0.005, -0.01, 0.01, 0.1 (0.1) 0.9), (b) Isotherms (θ : (0.005, 0.01 (0.01) 0.05, 0.55 (0.1) 0.85)

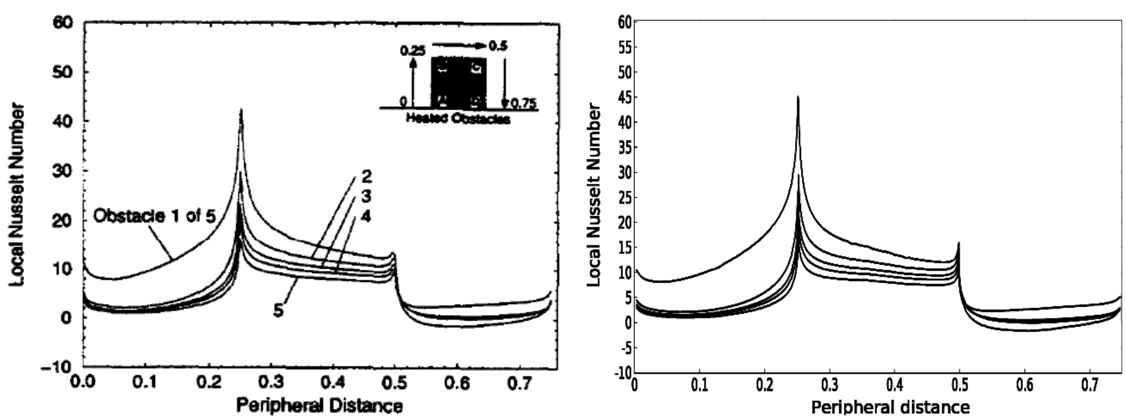

(a) (b)

Figure 1.4 Local Nusselt number distributions for the base line heat flux case: k_s/k_f=10 and Re=800, (a) results from Young and Vafai [25], (b) present work.

When porous barriers are mounted on the inside wall of the channel, our model is validated by comparsisons with the data from Fu et al. and Chikh et al. [10,11]. Fu [10] studied air passing through and around a single porous block with a height half of the width of the channel with *Re*=500. Moreover *Da* is set equal to 10^{-4} and the porous slab has the same conductivity as the air. The streamlines and isotherms generated through our simulations are compared with Fu's results in Figure 1.5. Again very good agreement is observed.

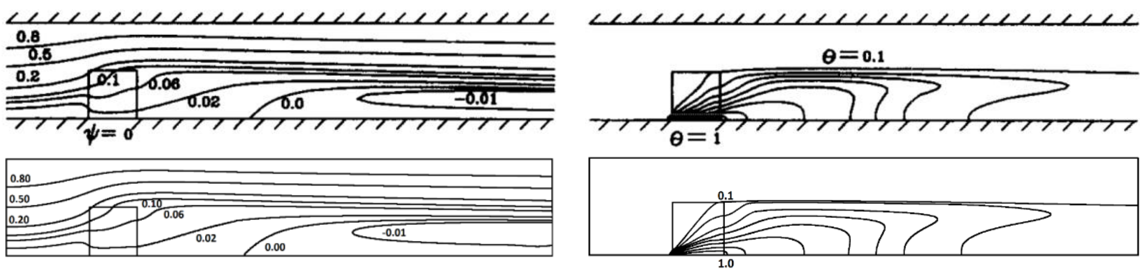

(a) (b)

Figure 1.5 Flow in a parallel plate channel, for $Da=10^{-4}$, $Pr=0.7$, $H^*=0.5$, $k_{eff}/k_f=1$ and $Re=500$, results from Fu et al. [10] located on top, and present work located on the bottom, (a) Streamlines (ψ :-0.01, 0.0, 0.02, 0.06, 0.1, 0.2, 0.5, 0.8) (b) Isotherms (θ : (0.1 (0.1) 1.0)

For further validation we compared our data with the numerical results of Chikh et al [11]. They considered an electronic cooling system comprised of a channel with multiple non-matallic porous structures installed on the heated region of the inside wall. Figure 1.6a demonstrates comparison of streamlines produced by our computational model with their work for three non-metallic porous blocks. The obstacles have heights equal to and half of the channel's height and widths similar to the channel's height. Air is the working fluid with *Re*=500 and the porous slab has these features: $Da=10^{-4}$, $\varepsilon=0.6$, $R_c=100$. Furthermore, Figure 1.6b compares the dimensionless wall temperature along the wall with heat sources for the same specifications mentioned above and for two values of Da=10^{-3} and 10^{-5} and also the case without the blocks. Also numbers calculated based on our computational model deviate from the data provided by Chikh et al., by less than 0.4%. As shown in Figures 1.3 to 1.6 our simulations yield velocity and temperature profiles in very good agreement with those of previously published studies.

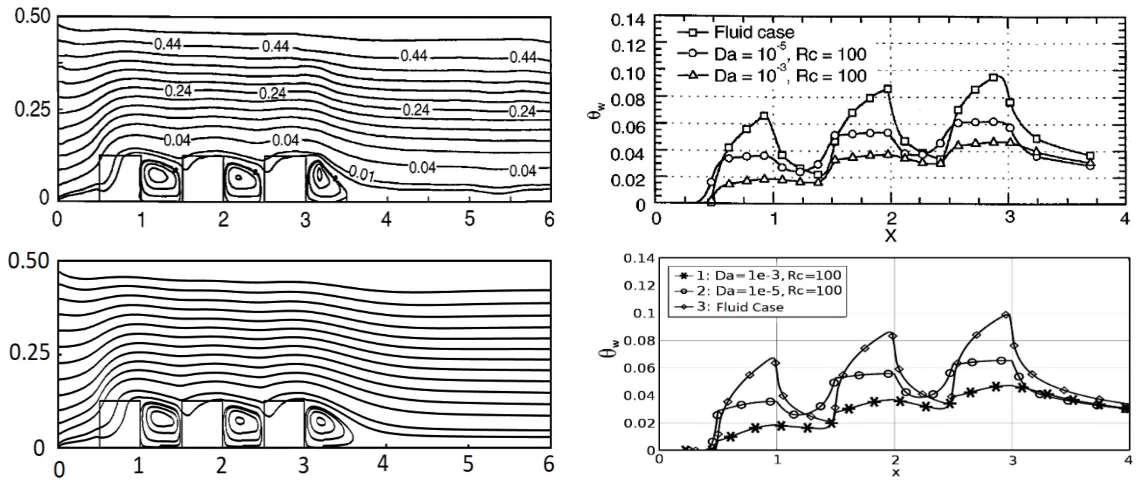

(a) (b)

Figure 1.6 Flow in a parallel plate channel for Da=10^{-4} and Re=500 and R_c=100, results from Chikh et al. [11] located on top, and present work located on the bottom, (a) Streamlines (b) Wall temperature.

6. Results and discussion

6.1 Single block

First we consider a single block attached inside the channel as shown in Fig. 1.1a, (L_h=R). Based on all the cases considered d_p^* has the most significant effect on the heat removal capacity of the system as well as the flow field formed inside the channel. For any specific fixed set of parameters, the porous structure acts nearly as a solid obstacle for d_p^*= 0.02. As we increase the average pore diameter to d_p^*= 0.1 and 0.2, the permeability of the porous medium increases proportionally and the flow increasingly penetrates into the metal foam. As such, the advantages of thermal interaction between fluid and the solid inside the porous domain with a high surface area comes into play. This can be seen in Figure 1.7 which demonstrates the streamlines for the case with a triangular block half of the height of the channel with ε=0.85 in a channel filled with air and Re=800.

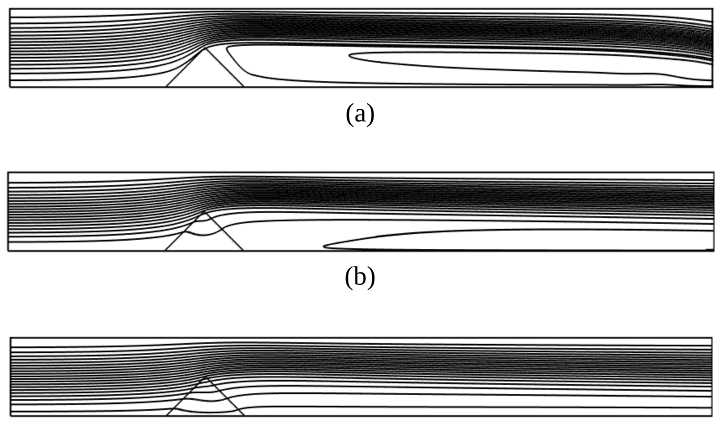

(a)

(b)

(c)

Figure 1.7 Streamlines for a single triangular Aluminum block with: AR=0.5, Pr=0.7, ε =0.85, for different values of (a) d_p^*=0.02, (b) d_p^*=0.1, (c) d_p^*=0.2.

The rectangular, triangular and elliptic geometries considered for comparison have the same height Aspect Ratio (AR) and width ratios (W^*) with respect to the height of the channel (R), See Fig. 1.1. For smaller values of d_p^* such as d_p^*=0.02 the rectangular shaped metal foams are most effective in removing heat from the heat source for a set pressure drop. This is illustrated in Figure 1.8 which demonstrates the Nusselt number enhancement ratio with respect to the average pressure drop augmentation ($\overline{\Delta P}/\overline{\Delta P_0}$) for two demonstrative specific cases. Figures 1.8a and 1.8b are representative cases for air and water respectively. Along each curve the value of Re increases from 200 to the transition point calculated based on the height of the gap between the block and the upper wall.

Therefore Re is embedded in the diagrams and each point on the curves represents a specific Re value, for which the corresponding pressure drop and Nusselt enhancement can be seen. In general the curves located to the left and upper areas of the plot, indicate more favorable conditions since they indicate less ΔP and more Nu enhancement.

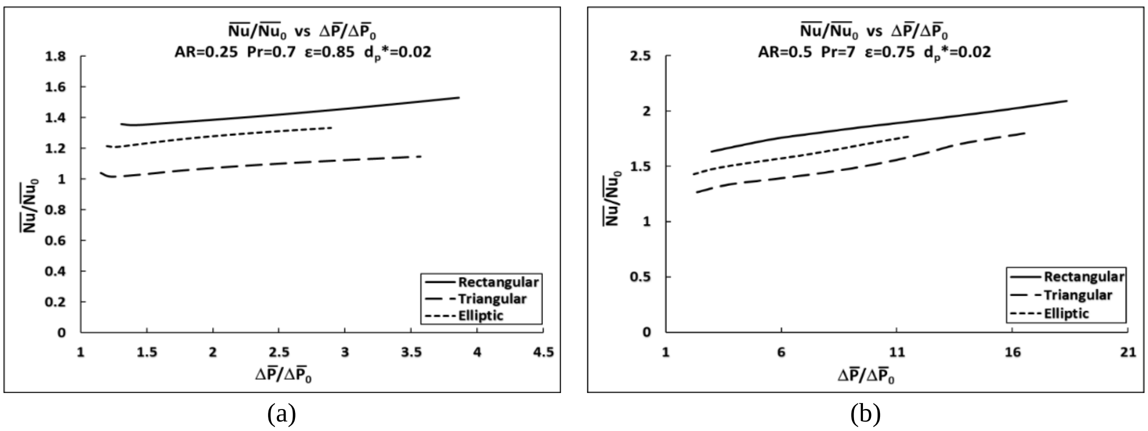

Figure 1.8 Comparing $\overline{Nu}/\overline{Nu_0}$ and $\overline{\Delta P}/\overline{\Delta P_0}$ for Aluminum blocks with small pores (d_p^* =0.02) and with different geometries, for both (a) air: Pr=0.7, K_r=8200 and (b) water: Pr=7, K_r=342 as the working fluid.

The results for d_p^*=0.02 are similar to cases with solid mounted blocks [28]. As can be seen in Figure 1.7a the streamlines mostly flow around the obstacle, therefore the outer surface area of the porous block plays the key role in the heat removal process. Among the shapes considered for very low d_p^* and consequently very low permeabilities, mounting triangular blocks cause the least, and rectangular blocks cause greatest increase in the surface area for interaction between the fluid and the heat source, respectively. Therefore higher surface area of rectangular obstacles along with direct interaction of the flow on their left walls makes them most effective.

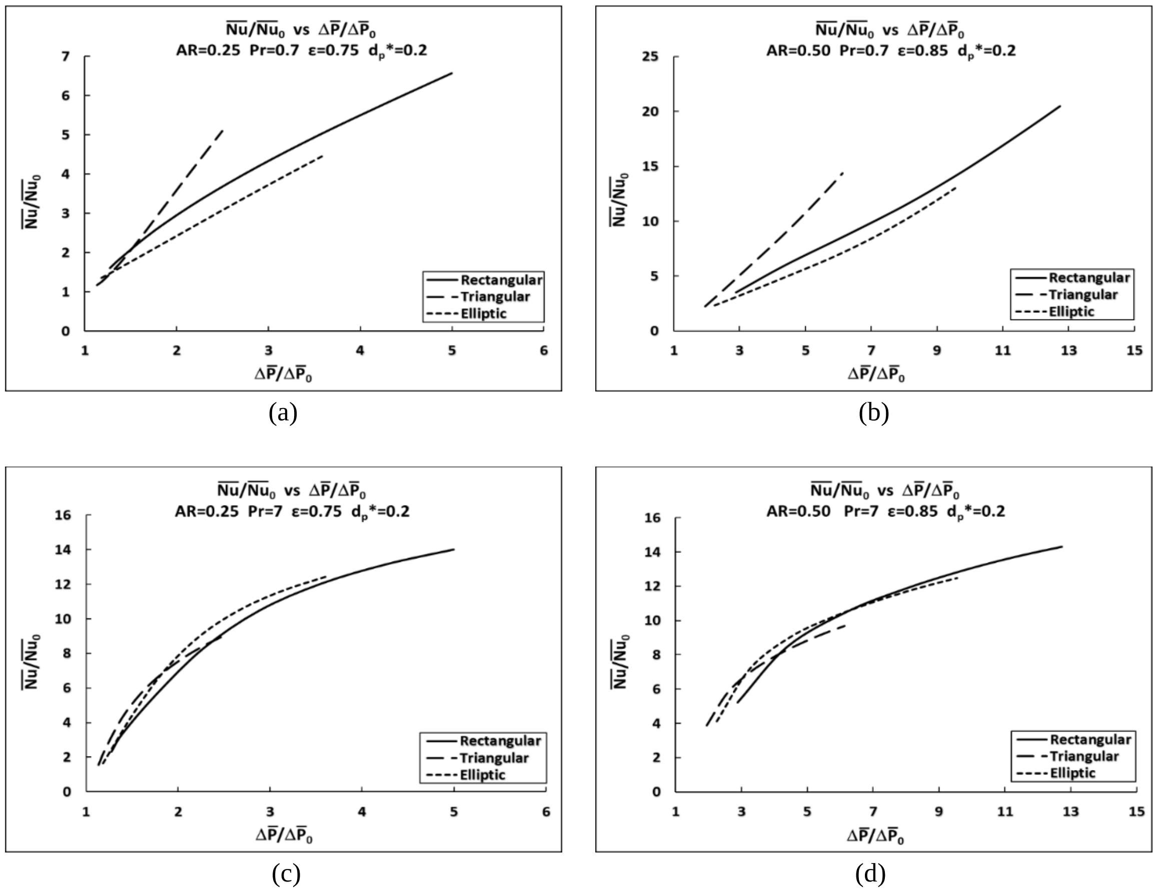

Figure 1.9 Comparing $\overline{Nu}/\overline{Nu_0}$ and $\overline{\Delta P}/\overline{\Delta P_0}$ for Aluminum blocks with d_p^* =0.2, 0.1 and different geometries, (a,b) with air as the working fluid (*Pr*=0.7, K_r=8200), (c,d) with water as the working fluid (*Pr*=7, K_r=342).

As we increase d_p^* to 0.1 and 0.2 the superior thermal features of the metal foam comes into play, causing much higher *Nu* enhancements, as can be seen in Figure 1.9. This situation is the main focus of this study and yields heat removal rates multiple times more than when the solid blocks are used or when d_p^*=0.02. Figures 1.9a and 1.9b demonstrate two demonstrative cases for a channel with air flowing inside, and as can be seen, triangular blocks are the most effective geometry especially at higher speeds (higher *Re*). This is due to the fact that it is easier for the flow to penetrate and pass through triangular blocks since the flow is facing a narrower vertical porous width along its path, hence lower ΔP ratios inside the block. For example, Figure 1.9b is for AR=0.5, ε=0.85 and d_p^*=0.2 and illustrates that a single triangular block can increase the heat removal 15 times with a 6 fold increase in ΔP. For a rectangular block with similar geometrical parameters and porous structure characteristics would yield a 10 fold increase in $\overline{Nu}/\overline{Nu_0}$ for the same pressure drop ratio.

When the working fluid is water, the effectiveness of different shapes are not significantly different. Figures 1.9c and 1.9d demonstrate three illustrative samples for this case. For example Figure 1.9c is for: AR=0.25, ε=0.75 and d_p^*=0.2, and as can be seen, both a rectangular and a triangular porous slab cause 9.5 times increase in average Nu with 2.5 increase in pumping power ratio. This conditions requires a Re=1300 for the triangular and Re=600 for the rectangular cases. Similarly an elliptic metal foam is causing marginally higher heat transfer increase for the same pressure drop conditions at Re=700. It is clear in this figure that rectangular and elliptic blocks cover a wider range of $\overline{Nu}/\overline{Nu_0}$. The higher end of this range contribute to extremely higher pressure drop values and is impractical. Since triangular geometry creates superior results for air and equally similar results for water compared to the other considered shapes, for the subsequent analysis of the various parameters involved, we will focus on the triangular barriers.

Figure 1.10 illustrates effects of porosity ε and non-dimensional mean pore diameter d_p^*, for air and water and for two different aspect ratios (AR) of the blocks, i.e., AR=0.25 and 0.5. Pore diameter and consequently Da has the most significant effect on the results and in all four diagrams, the curves are grouped based on d_p^*. As can be seen in all four diagrams, for $d_p^*=0.02$ results are very close to cases with solid blocks. Moreover higher d_p^* values such as 0.2 yield significantly better heat removal rates at the same $\overline{\Delta P}/\overline{\Delta P_0}$, compared to d_p^*=0.1. This trend holds true independent of the *AR* of the block. Moreover when the channel contains air (Figs. 1.10a and 1.10b) and all other parameters are fixed, including d_p^*, higher values of porosity produce moderately better heat removal results. Therefore for air in the channel the optimum curve is for d_p^*=0.2 and ε=0.95. On the other hand when water is flowing in the channel, ε=0.75 produces superior results compared to higher porosities. The optimum curves in Fig. 1.10c and 10d are for d_p^*=0.2 and ε=0.75.

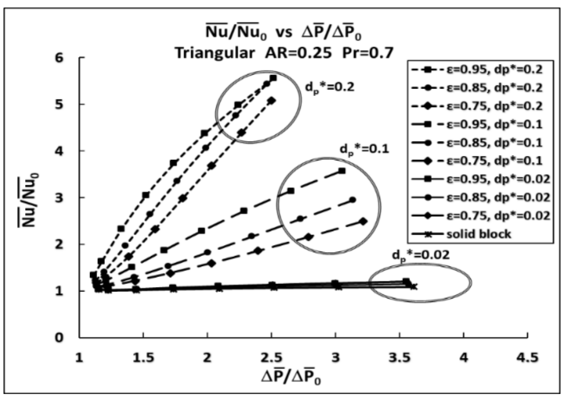

(a)

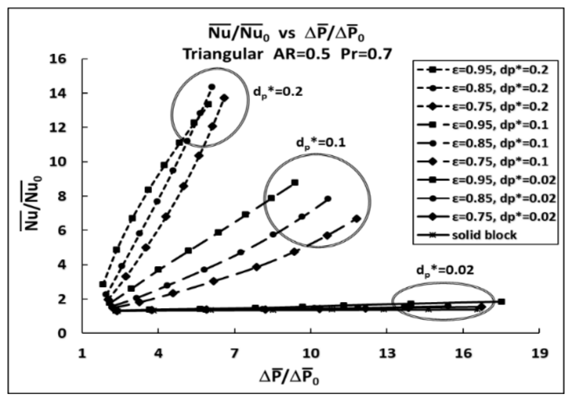

(b)

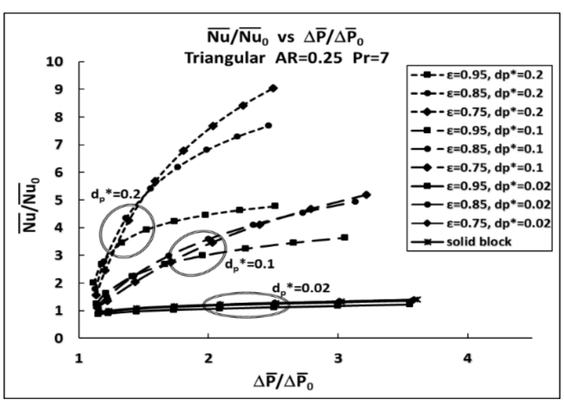

(c)

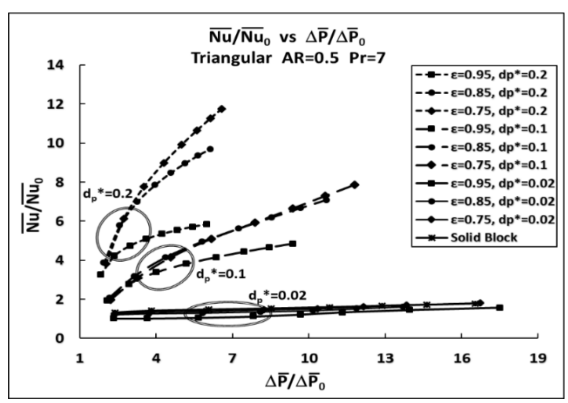

(d)

Figure 1.10 Effects of ε and d_p* of an Aluminum triangular block on $\overline{Nu}/\overline{Nu_0}$ and $\overline{\Delta P}/\overline{\Delta P_0}$ for the cases with air and water as the working fluid and aspect ratios: *AR*=0.25, 0.5.

It is important to note that, the effect of Forcheheimer coefficient (F), was investigated by fixing all the other parameters, and was found to have insignificant effect on the results compared to the other cited parameters. Therefore when we fix the value for ε, we are basically studying the effect of Darcy number (Da) by changing the non-dimensional mean pore diameter d_p^*. For instance, In Figure 1.10a the top curve in each of the groups correspond to ε=0.95 and the three values of d_p^* ranging from 0.02 to 0.2 correspond to Da=7.22×10^{-06} to Da=7.22×10^{-04}. Therefore d_p^* and Da are directly related and both have the most significant effect on the results.

To study the effect of the height Aspect Ratio of the porous block (AR), we consider d_p^*=0.2 and compare curves for ε=0.75, 0.95 for both air and water, as can be seen in Figure 1.11. If air is used, lower aspect ratios create higher thermal removal rates compared to taller blocks for the same values of $\overline{\Delta P}/\overline{\Delta P_0}$. At the same time the range of Nu enhancement which is covered in the laminar regime would become limited. For example, in Fig. 1.11a for average Nu ratio of 6, AR=0.3 is more efficient than taller counterparts due to lower corresponding pressure drops. This is while lower AR can't yield this enhancement within the laminar range.

The effect of the height aspect ratio of triangular blocks is more significant when water is flowing in the system. Fig. 1.11c and 1.11d demonstrate aspect ratios with values in excess of 0.2 substantially increase the $\overline{\Delta P}/\overline{\Delta P_0}$ ratio, while AR=0.2 yields almost the same enhancement in Nusselt number while keeping the pressure drop atwithin a reasonable range. Therefore values around AR=0.2 can create almost the same $\overline{Nu}/\overline{Nu_0}$ enhancement with a substantially smaller pressure drop penalty compared to taller slabs.

The *Nu* enhancement capacity of lower aspect ratio cases are not as significant as the ones for *AR*=0.2. Therefore values close to 0.2 can be considered as optimum for the relative height of the barrier to the height of the channel. In this work we chose *AR*=0.25 as a benchmark for the following analysis. For instance in Fig. 1.11c the curve for *AR*=0.2 shows $\overline{Nu}/\overline{Nu_0}$ values as high as 8 with an increase in the $\overline{\Delta P}/\overline{\Delta P_0}$ ratio, as small as 2. This is while in the same diagram *AR*=0.5 causes a modestly higher value of *Nu* enhancement of 11 but at the cost of 7 times increase in $\overline{\Delta P}/\overline{\Delta P_0}$.

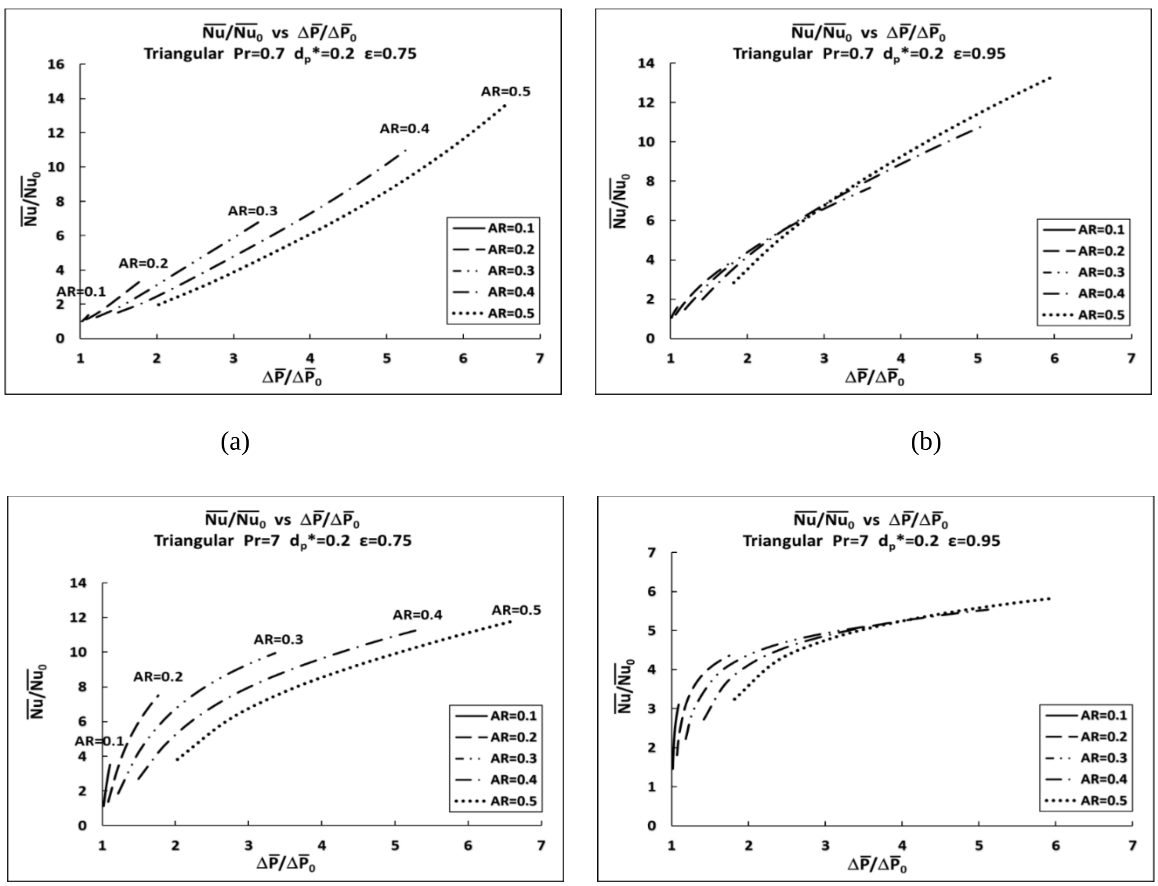

Figure 1.11 Effects of the height Aspect Ratio (*AR*) for an Aluminum triangular block with d_p^* =0.2, on $\overline{Nu}/\overline{Nu_0}$ enhancement and $\overline{\Delta p}/\overline{\Delta p_0}$ for the cases with air (a&b) and water (c&d) as the working fluid and porosities: ε=0.75 and 0.95.

By comparing the curves for $Pr=0.7$ and $Pr=7$ it is noticed that for lower porosity values (ε=0.75), Aspect ratios up to around 0.4 (Ar<0.4), water is more effective compared to air. This is while for Ar>0.4 (e.g. Ar=0.5) air flowing in the system is more effective in removing the heat. For instance in Fig. 1.11c for water, an aspect ratio equal to 0.2 can yield a maximum value of $\overline{Nu}/\overline{Nu_0}$ equal to 8 while in Fig. 1.11a for water the maximum heat transfer enhancement is $\overline{Nu}/\overline{Nu_0}=4$. While in the same two diagrams, the curve corresponding to air is located higher than the one for air. When the block has a high porosity (ε=0.95) Water is still more effective except only at pressure drop ratios higher than roughly three ($\overline{\Delta p}/\overline{\Delta p_0}=3$). These conclusions can also be noticed in Figure 1.10. Basically the downside of using water is creation of substantially higher pressure drops which can overtake its thermal advantages for some specific situations discussed earlier.

To check the local conditions of the system we choose the preceding optimum values found: d_p^*=0.2, ε=0.95 (Da=7.22×10^{-4}) and AR=0.25 for air and d_p^*=0.2, ε=0.75 (Da=2.48×10^{-4}) and AR=0.25 for water. In addition, we compare these two cases with smaller pore dimeters and ultimately to when the blocks are completely solid. Figures 1.13a and 1.14a display the average heat transfer and pressure drop enhancements for these cases. Other diagrams in Figures 1.13 and 1.14 demonstrate the local Nu enhancement and local Nu over the heated region as well as the non-dimensional wall temperature on the entire lower wall for two different Re values of 700 and 1400. Similar trends are noticed between diagrams for these two Re values (first and second row). It is clear that increasing Re, proportionally augments Nusselt values and decreases the maximum temperature of the wall. Similarities between the diagrams demonstrates that the comparative trends of the results stays the same at different *Re* numbers, while increasing *Re* intensifies these trends.

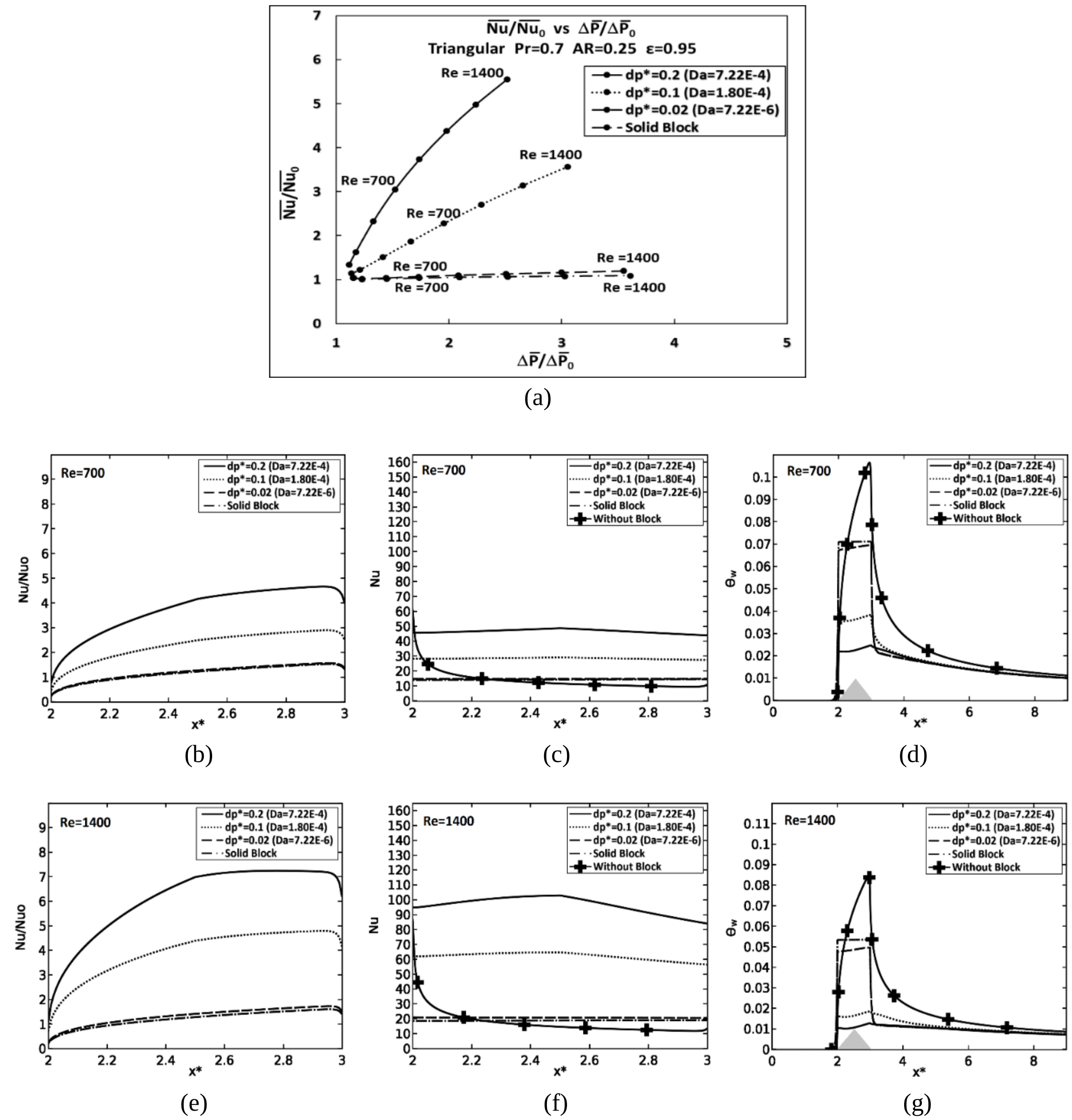

Figure 1.12 Triangular Aluminum foam with ε=0.95, *AR*=0.25 and air as the working fluid (*Pr*=0.7, K_r=8200), for different d_p^* values (a) $\overline{Nu}/\overline{Nu_0}$ versus $\overline{\Delta P}/\overline{\Delta P_0}$. (b, c, d) Local Nu/Nu_0 and *Nu* along the heated wall and Θ_w along upper wall for different d_p^* values at *Re*=700 and (e, f, g) *Re*=1400

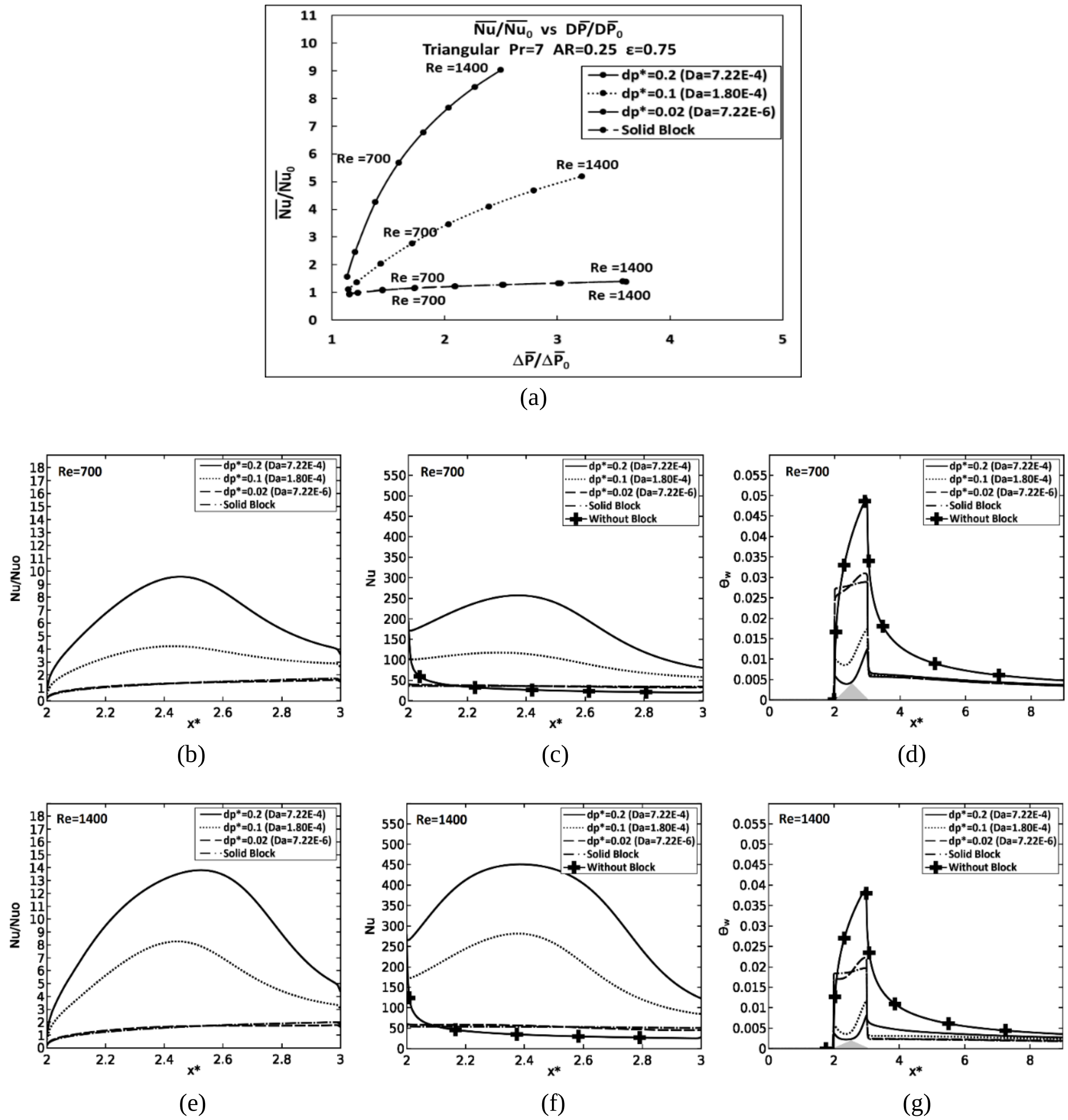

Figure 1.13 Triangular Aluminum foam with ε=0.75, *AR*=0.25 and water as the working fluid (*Pr*=7, K_r=342), for different d_p^* values (a) $\overline{Nu}/\overline{Nu_0}$ versus $\overline{\Delta P}/\overline{\Delta P_0}$. (b, c, d) Local Nu/Nu_0 and *Nu* along the heated wall and Θ_w along upper wall for different d_p^* values at *Re*=700 and (e, f, g) *Re*=1400

When there are no blocks present, local *Nu* is very high at the frontline where the flow reaches the heated region, and then right after, *Nu* values decrease drastically. This can be seen in Fig. 1.12c&f and 1.13c&f. When the metallic porous structures are introduced the thermal interaction occurs along the whole block and causes a relatively high local *Nu* all along the heated region, instead of just the far left of it. This redistribution of heat transfer causes overall higher $\overline{Nu} / \overline{Nu_0}$ values when a metal foam is introduced.

Figures 1.12d&g and 1.13d&g display that increasing d_p^* from 0.0 for solid blocks to 0.2 (and consequently increasing *Da*) substantially alters the temperature profiles on the lower wall. As a result the maximum non-dimensional temperature in considerably lower when the metallic foam heat sinks are introduced, while the location of this maximum stays at the end of the block. For example in Fig. 1.13g, when *Re*=1400, the maximum temperature is 1/8 of the pure solid block case. This outcome can be quite favorable especially in electronic cooling applications.

6.2 Single or multiple blocks:

6.2a) Air as the working fluid:

The thermal and flow features resulting from mounting a single or an array of metallic foam barriers on a heated region inside the channel have been analyzed. The heated region is long with respect to the height of the channel, L_h=6*R*. For this purpose 28 distinct and comprehensive sets of cases are introduced to cover various pertinent possible conditions. These cases are presented in Table 1.2 along with including their geometrical parameters for the barriers width and the distance between them. For all cases the height aspect ratio is considered as *AR*=0.25. The four columns from left to right include cases with *n*=1, 2, 3 and 4 blocks respectively. The first row in each column represents the situation that the whole heated zone is covered underneath the blocks. Other rows represent cases where the barriers partially cover the region with heat flux with different values of W^* and D^*.

Table 1.2 Dimensions (width and distance) of multiple obstacle cases investigated, for R=1 and H^*=0.25.

Case #	W^*	D^*	Case #	W^*	D^*	Case #	W^*	D^*	Case #	W^*	D^*
1 block			**2 blocks**			**3 blocks**			**4 blocks**		
1	6	0	8	3	0	15	2	0	22	1.5	0
2	1	5	9	1	2	16	1	1	23	1	0.5
3	0.5	5.5	10	0.5	2.5	17	0.5	1.5	24	0.5	1
4	0.25	5.75	11	0.25	2.75	18	0.25	1.75	25	0.25	1.25
5	0.125	5.875	12	0.125	2.875	19	0.125	1.875	26	0.125	1.375
6	0.05	5.95	13	0.05	2.95	20	0.05	1.95	27	0.05	1.45
7	0.02	5.98	14	0.02	2.98	21	0.02	1.98	28	0.02	1.48

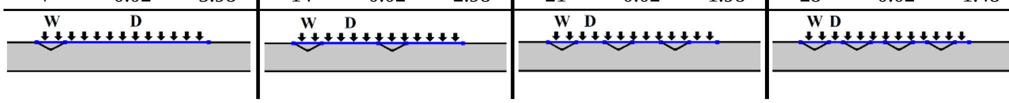

Based on our results, metal foams become effective as d_p^* increases to 0.1 and 0.2, and therefore d_p^* and consequently Da have a dominant effect, as discussed earlier. The best Nu enhancement with minimum $\overline{\Delta p} / \overline{\Delta p_0}$ occurs for blocks with triangular geometries especially for the case of air ($Pr=0.7$). Higher porosities are favorable for air and ε=0.75 is more favorable for water, and increasing Re intensifies the effects on both Nu and ΔP. These conclusions can be seen in Figure 1.14 which demonstrates the effects of shape and porosity for cases 2 and 24 for both air and water. All four diagrams are for d_p^*=0.2 which is the optimum value. In Figures 1.14a&b the channel is filled with air and shows how triangular metal foams are the best option. Nevertheless, In Figures 1.14 c&d which are for water, the effect of shape is not significant while ε=0.75 clearly yields superior results, similar to a single block situation.

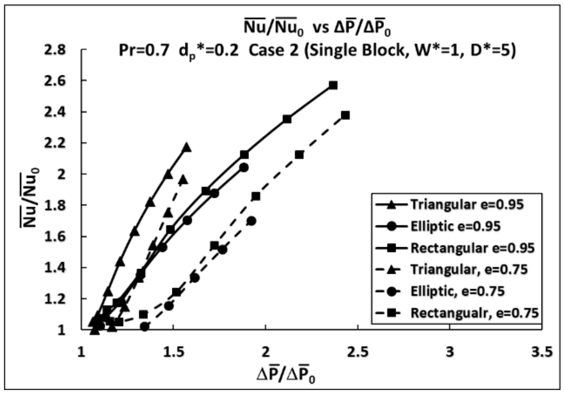

(a)

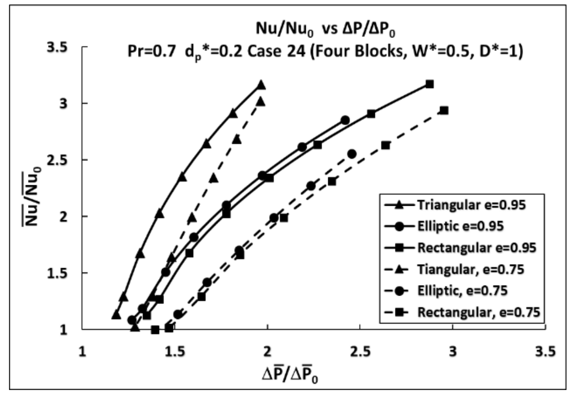

(b)

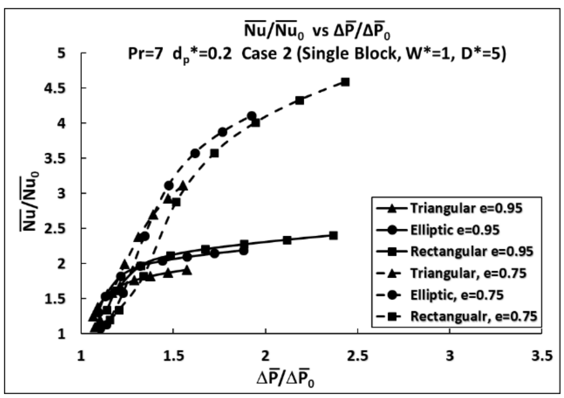

(c)

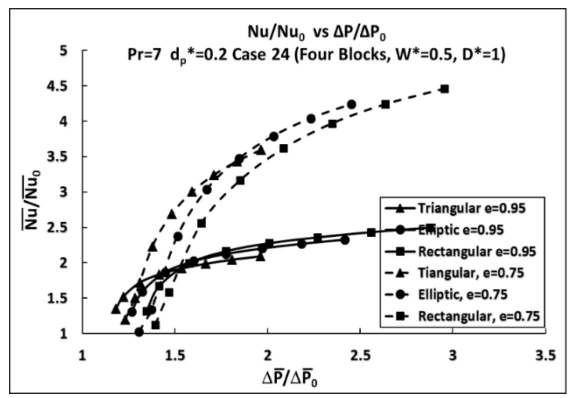

(d)

Figure 1.14 Effects of ε (ε=0.75 and 0.95) and geometry for two representative cases 2 and 24 with aluminum triangular blocks, for d_p^* =0.2 and AR=0.25, on $\overline{Nu}/\overline{Nu_0}$ and $\overline{\Delta P}/\overline{\Delta P_0}$ for (a, b) air: Pr=0.7, K_r=8200 and (c, d) water: Pr=7, K_r=342 as the working fluid.

The effect of the geometrical parameters W^* and D^* along with the number of blocks utilized are shown in Figure 1.15. In all four diagrams the case for which the whole wall is roofed by the blocks (solid line), yields the highest pressure drop ratio with relatively small average Nu ratio gains. Also whenever $W^*$of the blocks is smaller than 0.1 (the two curves on far left in each of the four diagrams) the maximum heat transfer augmentation is limited in the laminar region that is studied in this work. Overall, for fixed number blocks, W^* values from 0.125 to 0.5 yield maximum heat transfer with reasonably small pressure drops. For example in Fig. 1.15c, three sequentially spaced blocks each with a width of a quarter of the channel height, cause 3 times increase of $\overline{Nu}/\overline{Nu_0}$ for 1.5 times increase in $\overline{\Delta P}/\overline{\Delta P_0}$.

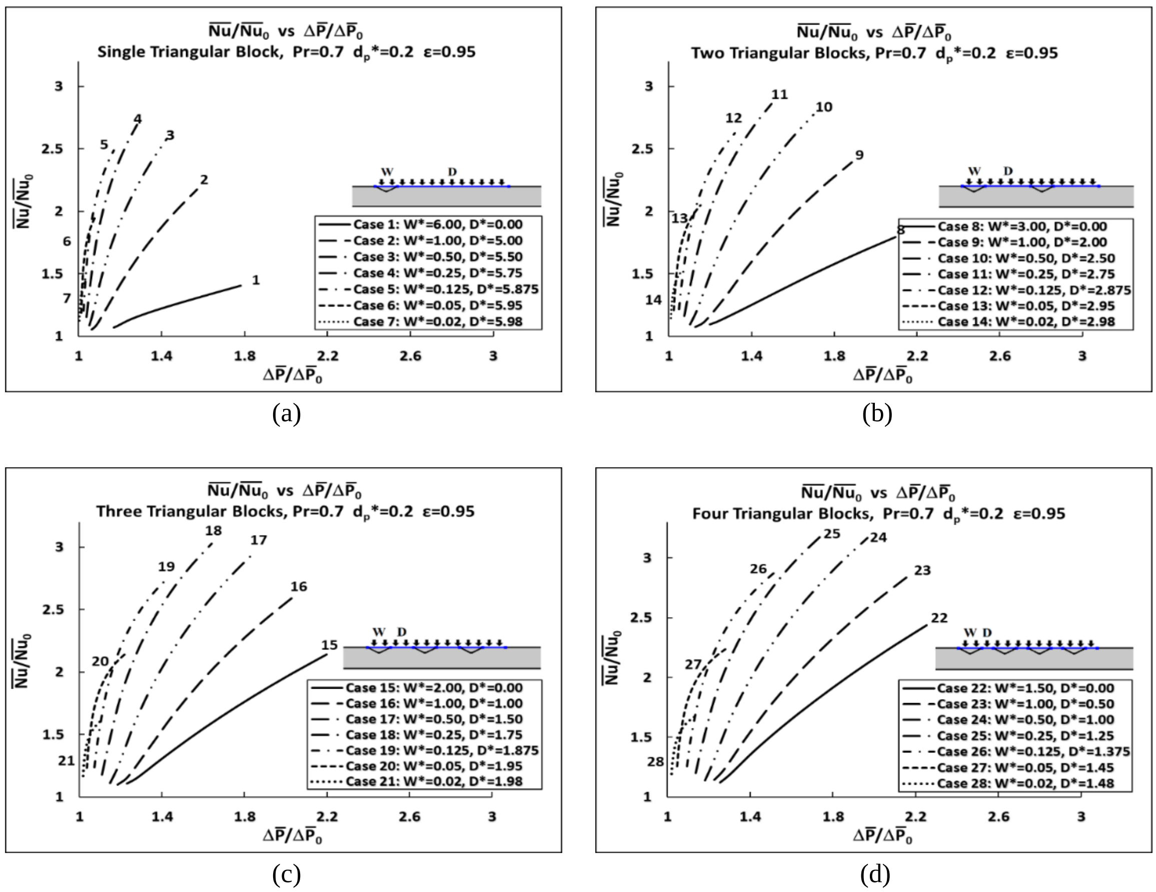

Figure 1.15 Effects of width (W^*) and distance (D^*) of an array of triangular blocks with ε=0.95, d_p^* =0.2, AR=0.25, for air flow in the channel: Pr=0.7, K_r=8200, on $\overline{Nu}/\overline{Nu_0}$ and $\overline{\Delta P}/\overline{\Delta P_0}$ for the cases with (a) 1 block, (b) 2 blocks, (c) 3 blocks, (d) 4 blocks.

By fixing the value for the width ratio, we can study the effect of the number of barriers on the thermo-fluid characteristics of the system. Figure 1.16 illustrates the comparison of the average Nu and ΔP enhancements, with regards to Number of blocks, for different values of W^*.

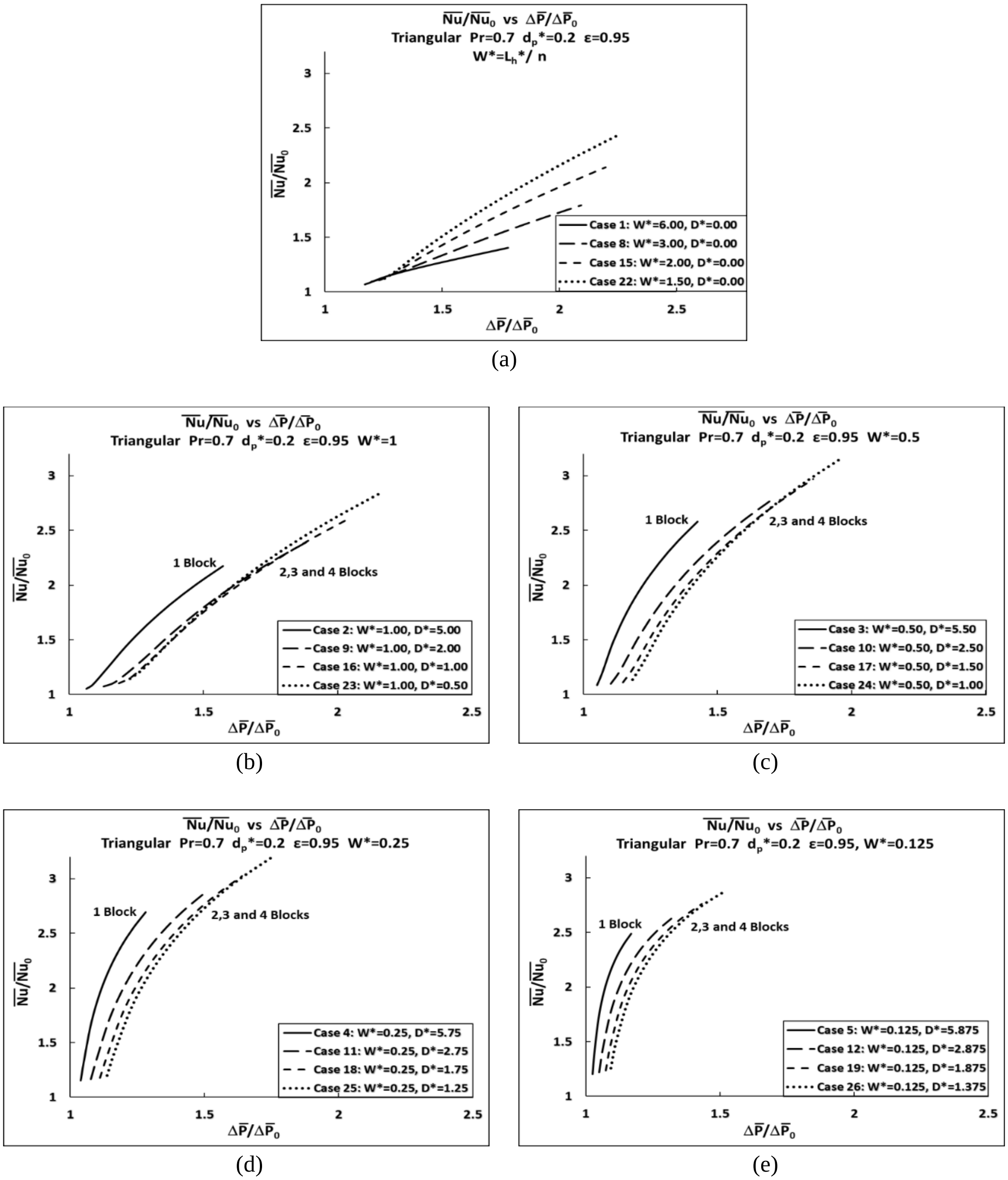

Figure 1.16 Effects of number of triangular blocks with ε=0.95, d_p^* =0.2 and AR=0.25 mounted in a channel for air flow: Pr=0.7, K_r=8200, on $\overline{Nu}/\overline{Nu_0}$ and $\overline{\Delta P}/\overline{\Delta P_0}$ for fixed values of W: (a) W^*=L_h^*/n (b) W^*=1 (c) W^*=0.5 (d) W^*=0.25 (e) (d) W^*=0.125

Figure 1.16a depicts that amongst the cases in which the metal foam covers the entire heated region (cases 1,8,15,22), increasing the number of blocks is advantageous with regards to the average *Nu* and ΔP enhancement ratios. But when the heated region is partially covered, the behavior of the system is different, and in Figs. 1.16b to 1.16d, it can be seen that increasing the number of blocks slightly improves the heat removal capacity at the cost of significant pressure drop. Therefore, when the heated region is partially covered, using a single metallic porous slab is more effective than using several blocks with the same widths. Amongst all the considered cases with air as the working fluid a single block with a width roughly a quarter of the channel height (Fig. 1.16d) is the most effective, and can increase $\overline{Nu}/\overline{Nu_0}$ by a factor of 2.7 while only increasing the $\overline{\Delta P}/\overline{\Delta P_0}$ by 30%. It should be noted that if an average *Nu* augmentation in excess of 2.7 is needed, it can be acquired by means of adding extra blocks to moderately improve heat transfer capacity, but at the cost of significant extra pressure drop.

6.2b) Water as the working fluid:

Same Figure 1.17 demonstrates effect of W^* for four fixed number of barriers in each of the four diagrams for water flow through the channel. It can be seen that for pressure drop ratios larger than 1.3 it is best to have the entire heated region covered under the porous slabs. For example, for the case of one block (Fig. 1.17a) if pressure drop ratio of 1.3 can be afforded, it is best to have that block cover the entire heated region. The same can be said with two or more barriers. For $\overline{\Delta P}/\overline{\Delta P_0}$ values less than 1.3 but the maximum average *Nu* enhancement is reduced drastically.

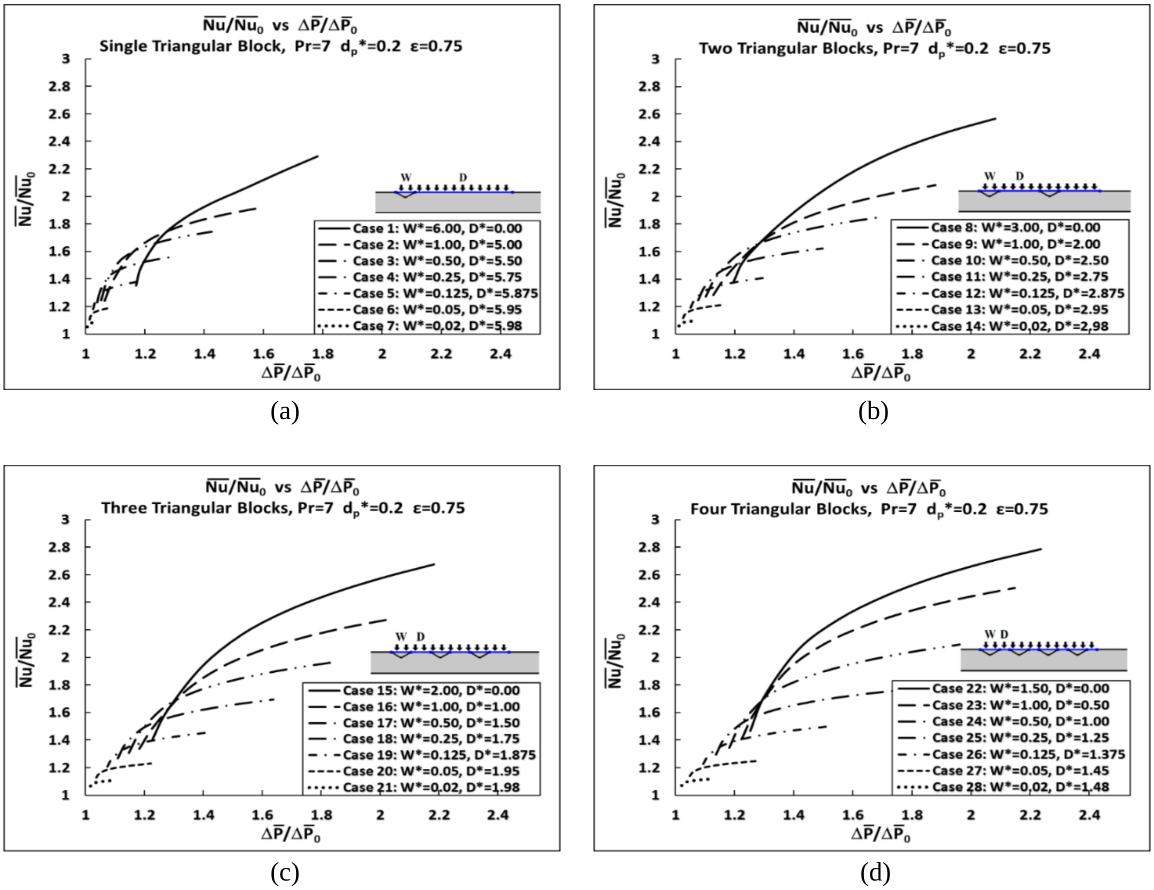

Figure 1.17 Effects of width (W^*) and distance (D^*) of an array of triangular blocks with ε=0.75, $d_p{}^*$ =0.2, AR=0.25, for water flow in the channel: Pr=7, K_r=342, on $\overline{Nu}/\overline{Nu_0}$ and $\overline{\Delta P}/\overline{\Delta P_0}$ for the cases with (a) 1 block, (b) 2 blocks, (c) 3 blocks, (d) 4 blocks.

In contrast to the cases where air was the working fluid, when water is used, a single block is not always the best option. For pressure drop values smaller than 1.3 single block is most effective while for pressure drop ratios in excess of 1.3 having more blocks is more efficient. This can be verified in Figure 1.18 which demonstrates the effect of number of blocks for fixed values of W^* in each of the four diagrams. All things considered if $\overline{\Delta p}/\overline{\Delta p_0}$ decreases from 1.3 a single block with decreasing width is favorable; and in $\overline{\Delta p}/\overline{\Delta p_0}$ values higher than 1.3 the more the number of the blocks in a setting covering the whole heated area is the best.

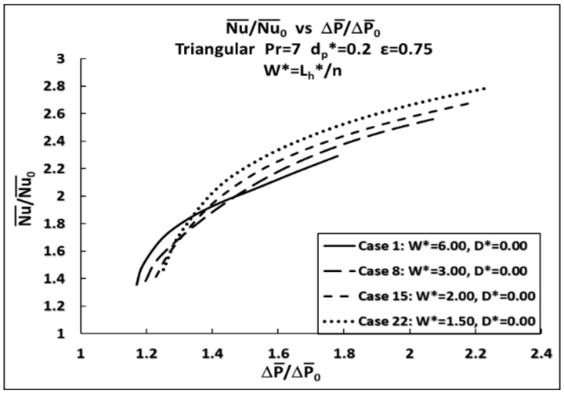

(a)

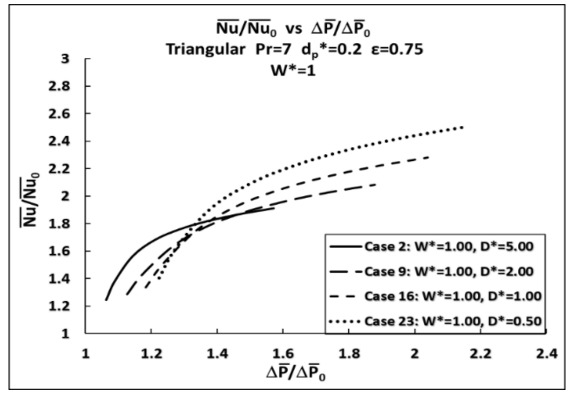

(b)

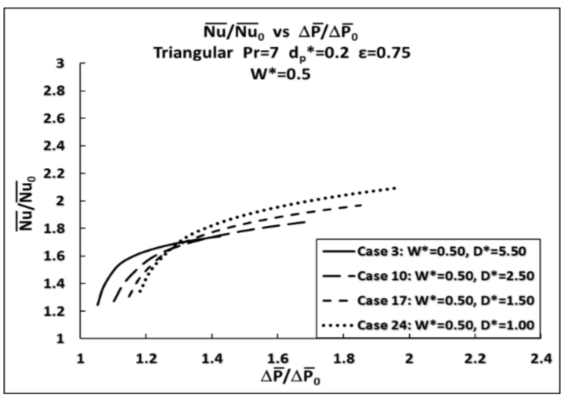

(c)

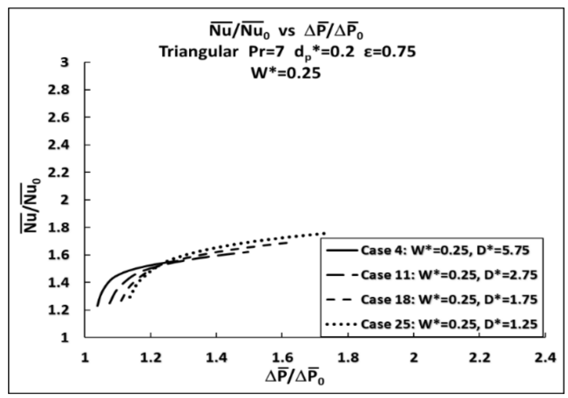

(d)

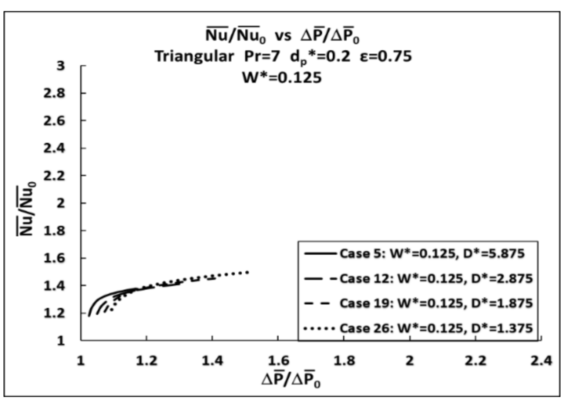

(e)

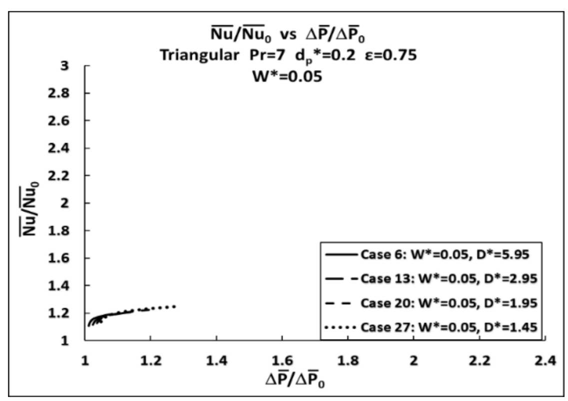

(f)

Figure 1.18 Effects of number of triangular blocks with ε=0.75, d_p^* =0.2 and *AR*=0.25 mounted in a channel for water flow: *Pr*=7, K_r=342, on $\overline{Nu}/\overline{Nu_0}$ and $\overline{\Delta p}/\overline{\Delta p_0}$ for fixed values of W: (a) $W^*=L_h/2$ (b) W^*=1 (c) W^*=0.5, (d) W^*=0.25, (e) W^*=0.125 (f) W^*=0.05.

Figures 1.19 and 1.20 demonstrate local circumstances for air (Fig. 1.19) and water (Fig. 1.20) at two specific *Re* number values of 700 and 1400. Figure 1.19 is for case 20 with 4 aluminum porous blocks with $W^*=0.5$ and $D^*=1$ while Fig. 1.20 represents case 22 with four blocks with $W^*=1.5$ adjacent to each other. Figs. 1.19a and 1.20a show how the *Nu* ratio of the first block is larger than the other ones. Also in Figs. 1.19b and 1.20b it is clear that the area between the *Nu* curves for d_p^* =0.2 and no blocks is much larger for the first block compared to the ones downstream and d_p^* =0.2. In this diagram, when there are no blocks mounted *Nu* has a high value in the close vicinity at the beginning of heated region at x^*=2, while adding the first block yield high *Nu* values all throughout the wall.

First block has the most significant role in heat removal, and its optimum location is right at the beginning of the heated region of the wall. This is due to the higher temperature difference between the wall and the adjacent layers of fluid, compared to other regions of the heated surface (as seen in Fig. 1.3b). Also as can be seen in the flow fields displayed in Figures 1.3a and 1.6a, substantially higher flow rates passes through the first block compared to the other blocks. This is partly due to the recirculation zones between the blocks. This greater intrusion of flow within the first block also contributes to the heat transfer enhancement in this area and is another reason for superior effectiveness of the first block.

Moreover in Figures 1.19d&g and 1.20d&g it can be seen that increasing d_p^* and consequently *Da* values results in an increase in the overall wall temperature curves. Nevertheless, an array of metallic foam heat sinks do not necessarily lower the maximum temperature compared to the case of a plain channel, as they cause peaks in temperature right at the end of each block (Fig. 1.19d&g and Fig 1.20d&g). At the same time the blocks on the average lower the wall temperature due to distributing the heat exchange process throughout the metallic porous medium.

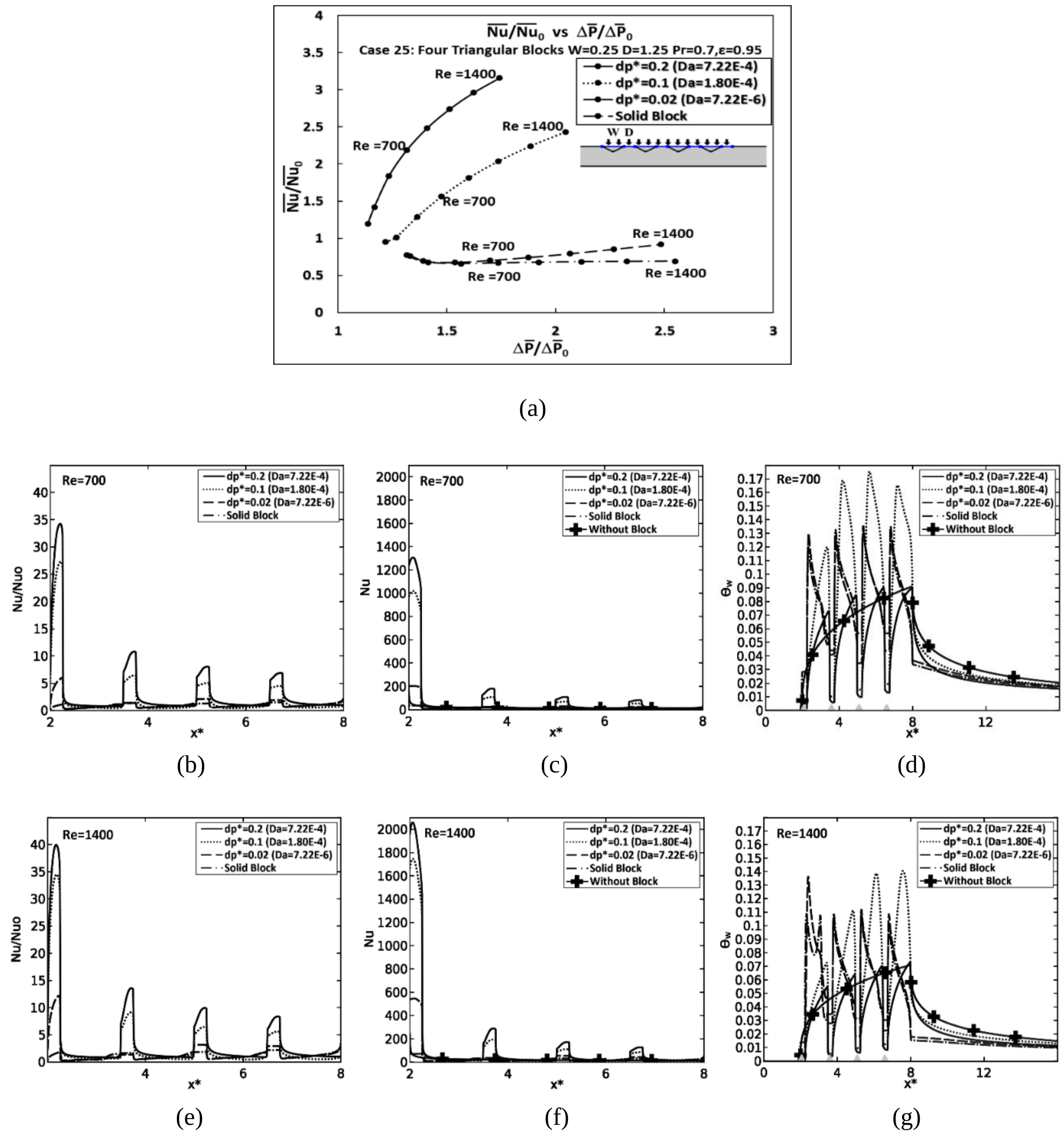

Figure 1.19 Case 25 with triangular Aluminum foam with ε=0.95, *AR*=0.25 and air as the working fluid (Pr=0.7, K_r=8200). (a) $\overline{Nu}/\overline{Nu_0}$ versus $\overline{\Delta P}/\overline{\Delta P_0}$. (b, c, d) Local Nu/Nu_0 and Nu along the heated wall and Θ_w along upper wall for different d_p^* values at Re=700 and (e, f, g) Re=1400

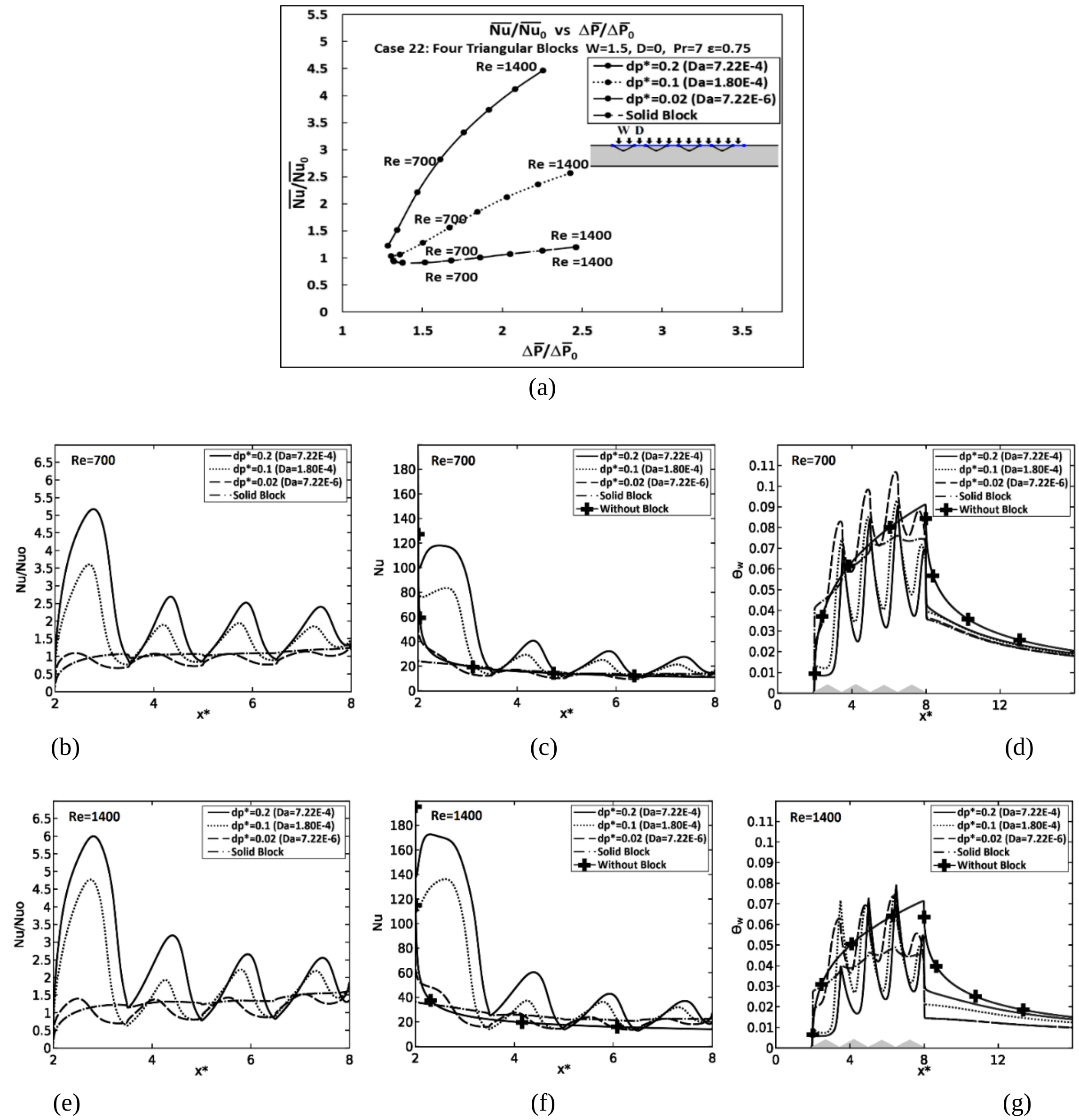

Fig 1.20 Case 22 with triangular Aluminum foam with ε=0.75, *AR*=0.25 and water as the working fluid (Pr=7, K_r=342). (a) $\overline{Nu}\,/\,\overline{Nu}_0$ versus $\overline{\Delta p}\,/\,\overline{\Delta p}_0$. (b, c, d) Local Nu/Nu_0 and Nu along the heated wall and Θ_w along upper wall for different d_p^* values at Re=700 and (e, f, g) Re=1400

It is worth mentioning in all of our investigations, the optimum case is explored, based on considering both the pumping power and the heat transfer augmentation. If in a design project with insignificant restrictive limitation for the pumping power, the best results could be simply found by extracting the maximum values of $\overline{Nu} / \overline{Nu_0}$ in the corresponding proposed diagrams. Also it should be noted that metals other than Aluminum would have different conductivities, and the higher the conductivity of the solid material the heat transfer rates would be higher but with the same qualitative characteristics presented through our investigations. Therefore the results from our research can be extended for metal foams other than aluminum based ones as well.

7. Conclusions

Thermal performance of a metal foams attached in a partially heated channel is examined in detail, considering the pertaining thermal and flow characteristics in the fluid and the porous domains. Based on our results the following conclusions can be expressed for the cases when the porous block covers the heated section which is about the same as the height of the channel:

1. The mean pore diameter d_p^* and consequently the Darcy number Da have the most dominant effect on the thermos-fluidic efficiency of the system. The superior heat removal capacity of the porous blocks prevails as d_p^* increases to 0.1 and 0.2.
2. When air is the working fluid, the best Nu enhancement ratios are acquired for triangular shaped metal foams, both for single and array settings. The shape does not play a key role when water flows in the channel.
3. When air is used, increasing the porosity (ε) augments the heat removal capacity, while lower porosity metal foams are more favorable when water is used as the working fluid.

4. Optimum height of the triangular obstacles is roughly 1/5 of the channel height both for single and array cases, while taller obstacles can yield higher average *Nu* enhancement but it will create a substantially higher pressure drop.
5. A single block is capable of significantly lowering the maximum temperature of the heated surface (e.g. up to 1/8 of the case without obstacles at high *Re* numbers).

The following conclusions can be drawn regarding cases with single or array of porous blocks, fully or partially covering the heated section:

1. The first block plays the prominent role in the heat removal process and its optimum position is right at the outset of the heated section.
2. When air is the working fluid, the optimum order is to place a single obstacle with a width roughly a quarter of the channel's height.
3. When water is the working fluid, the optimal results are achieved, with an increased number of obstacles covering the entire heated section.
4. When the heated section is long compared to the height of the channel, a single block partially covering the heat source or an array setting do not necessarily reduce the maximum wall temperature, however the average temperature of the heated surface still diminishes. Therefore when the maximum temperature is the design parameter, a single block covering the whole heat source would be desirable.

References

[1] C. C. Wang, C. K. Chen, Forced convection in a wavy-wall channel, Int. J. Heat Mass Transfer, vol. 45, no. 12, pp. 2587-2595, 2002.

[2] A. albojamal, H. Hamzah, A. Haghighi and K. Vafai, Analysis of nanofluid transport through a wavy channel, Num. Heat Transfer, Part A: Applications, pp 1-22, 2017.

[3] F. Chabane, N. Hatraf, N. Moummi, Experimental study of heat transfer coefficient with rectangular baffle fin of solar air heater, Front. Energy, Vol. 8, no. 2, pp. 160–172, 2014.

[4] A. I. Kudish, E. G. Evseev, G. Walter, T. Leukefeld, Simulation study of a solar collector with a selectively coated polymeric double walled absorber plate, Energy Conversion and Management, Vol. 43, no. 5, pp. 651–671, 2002.

[5] D. Y. Lee, K. Vafai, Analytical characterization and conceptual assessment of solid and fuid temperature differentials in porous media, Int. J. Heat Mass Transfer, Vol. 42, no. 3, pp. 423-435, 1999.

[6] K. S. Reddy, G.V. Satyanarayana, Numerical Study of Porous Finned Receiver for Solar Parabolic Trough Concentrator, Engineering applications of computational fluid mechanics, vol. 2, no. 2, pp. 172-184, 2008.

[7] J.C.Y. Koh, R. Colony, Analysis of cooling effectiveness for porous material in a coolant passage, ASME J. Heat Transfer, vol. 96, no. 3, pp. 324–330, 1974.

[8] M. Kaviany, Laminar flow through a porous channel bounded by isothermal parallel plate, Int. J. Heat Mass Transfer, vol. 28, no. 4, pp. 851–858, 1985.

[9] P.C. Huang, K. Vafai, Analysis of forced convection enhancement in a parallel plate using porous blocks, AIAA J. Thermophys. Heat Transfer, vol. 8, pp. 563– 573, 1994.

[10] W. Fu, H. Huang, W. Liou, Thermal enhancement in laminar channel flow with a porous block, Int. J. Heat Mass Transfer, vol. 39, no.10, pp. 2165–2175, 1996.

[11] S. Chikh, A. Boumedien, K. Bouhadef, G. Lauriat, Analysis of fluid flow and heat transfer in a channel with intermittent heated porous blocks, Heat and Mass Transfer, vol. 33, no. 5-6, pp. 405–413, 1998.

[12] J. Banhart, Manufacture, characterisation and application of cellular metals and metal foams, Progress in Materials Science, Vol. 46, no. 6, pp. 559–632, 2001.

[13] C. Y. Zhao, Review on thermal transport in high porosity cellular metal foams with open cells, Int. J. Heat Mass Transfer, Vol. 55, no. 13-14, pp. 3618–3632, 2012.

[14] S. Mahjoob and K. Vafai, A synthesis of fluid and thermal transport models for metal foam heat exchangers, Int. J. Heat Mass Transfer, vol. 51, pp. 3701-3711, 2008.

[15] S.Y. Kim, J.W. Peak, B.H. Kang, Thermal performance of aluminum-foam heat sinks by forced air cooling, IEEE Trans. Compon. Pack. Technol, vol. 26, pp.262– 267, 2003.

[16] K.C. Leong, L.W. Jin, Characteristics of oscillating flow through a channel filled with open cell metal foam, Int. J. Heat Fluid Flow, vol. 27, no. 1, pp. 144–153, 2006.

[17] K. Boomsma, D. Poulikakos, and F. Zwick, Metal foams as compact high performance heat exchangers, Mechanics of materials, Vol. 35, no. 12, pp. 1161-1176, 2003.

[18] D. Angirasa, Forced convective heat transfer in metallic fibrous materials, ASME J. Heat Transfer, vol. 124, no. 4, pp. 739–745, 2002.

[19] A. Bhattacharya, R.L. Mahajan, Finned metal foam heat sinks for electronics cooling in forced convection, J. Elect. Packag., vol. 124, no. 3, pp. 155–163, 2002.

[20] K. Vafai and C. L. Tien, Boundary and Inertia effects on Flow and Heat Transfer in Porous Media, Int. J. Heat Mass Transfer, vol. 24, no. 2, pp. 195–203, 1981.

[21] M. Kaviany, Boundary layer treatment of forced convection heat transfer from a semi-infinite flat plate embedded in porous media, Journal of Heat Transfer, vol. 109, no. 2, pp. 345–349, 1987.

[22] K. Vafai and S. J. Kim. Analysis of surface enhancement by a porous substrate, ASME J. Heat Transfer, vol. 112, no. 3, pp. 700–705, 1990.

[23] S. B. Sathe. W. Q. Lin and T. W. Tong, Natural convection in enclosures containing an insulation with a permeable fluid-porous interface. Int. J. *Heat Fluid Flow*, vol. 9, no. 4, pp. 389–395, 1988.

[24] N. Dukhan, Ed. Metal foams: fundamentals and applications. DEStech, Lancaster, PA, 2013.

[25] V. V. Calmidi, Transport phenomena in high porosity metal foams, Ph.D. Thesis, University of Colorado, Boulder, CO, 1998

[26] A. Bhattacharya, V. V. Calmidi, R. L. Mahajan, Thermophysical properties of high porosity metal foams, Int. J. Heat Mass Transfer, vol. 45, no. 5, pp. 1017–1031, 2002.

[27] T. J. Young, K. Vafai, Convective flow and heat transfer in a channel containing multiple heated obstacles, Int. J. Heat Mass Transfer, vol. 41, pp. 3279–3298, 1998.

[28] T. J. Young, K. Vafai, Convective cooling of a heated obstacle in a channel, Int. J. Heat Mass Transfer, vol. 41, no. 20, pp. 3131–3148, 1997.

CHAPTER 2: Optimal Positioning of Strips for Heat Transfer Reduction within an Enclosure

Nomenclature:

A	aspect ratio ($= H / W$)
D_x	location of vertical partition ($= x / W$)
D'_x	dimensionless distance of vertical partition from the left wall
D_y	location of horizontal partition ($= y / H$)
D'_y	dimensionless distance of horizontal partition from the bottom wall
g	gravitational acceleration, [m / s^2]
H	height of enclosure, [m]
h	local heat transfer coefficient, [$W / m^2 K$]
k	thermal conductivity, [W / mK]
L	dimensionless length of partition, ($= L' / H$ or L' / W)
L'	length of partition, [m]
Nu	local Nusselt number
$\overline{Nu}$	average Nusselt number
Pr	Prandtl number
p'	local pressure, [N / m^2]
p	dimensionless pressure
Ra	Rayleigh number

R_r Nusselt number reduction ratio

T dimensionless temperature

T' local temperature, [K]

t dimensionless thickness of partition

t' thickness of partition, [m]

u, v dimensionless velocity components

u', v' local velocity components

W width of enclosure, [m]

x', y' dimensional Cartesian coordinates

x, y dimensionless Cartesian coordinates, ($= x'/W, y'/H$)

Greek symbols:

α thermal diffusivity coefficient, [m^2/s]

β thermal expansion coefficient, [$1/K$]

ν momentum diffusivity of fluid, [m^2/s]

ρ density of the fluid, [kg/m^3]

ψ dimensionless streamfunction

ψ' dimensional streamfunction

Subscripts:

C cold wall

H hot wall

p partition

1. Introduction:

Natural convection heat transfer through air filled cavities of different geometries is a classical problem which has received great deal of attention, due to its special theoretical and practical importance. This problem has a wide variety of engineering applications including cooling electronics devices, designing heat exchangers and solar thermal collectors, heating and ventilating applications and energy conservation in refrigeration units. Comprehensive reviews on the subject have been written by Catton [1], Ostrach [2] and Jaluria [3]. In many applications obstructions of different shapes and orientations are fixed in the enclosure with the main purpose of adjusting the flow and heat transfer characteristics of the cavity, by modifying the flow and temperature fields of the system [4-52].

Various wall and partition conditions have been investigated in the literature numerically [5-15]. Zimmerman and Acharya [12] presented a numerical simulation of natural convection in a square cavity with perfectly conducting horizontal walls, and with conductive dividers. They accounted for the effects of thickness and conductivity of the baffle. Frederick et al. [34] studied the same problem with a partition at the center of the hot wall and investigated the effect of partitions length and conductivity. Acharya and Jetli [14] extended this work by taking into consideration the effects of the location and height of the partition and also end wall conditions on the heat transfer characteristics of the enclosure. Chen and Ko [15] presented a numerical study for the case of a rectangular enclosure, with $A = 2$ and a partition ratio of 1/2 with an opening, in which two side walls were maintained at uniform heat flux condition and the top and bottom walls were insulated. They observed that the partition opening, rather than the conductivity, significantly influences the overall heat transfer.

Nag et al. [16] investigated the effect of a horizontal thin plate with infinite or zero thermal conductivity, positioned on the hot wall of the square cavity while length and location of the partition were variable. They reported that an adiabatic partition reduced heat transfer especially when located close to the ceiling, due to blocking the convection currents. Shi and Khodadadi [17] and Tasnim and Collins [18] studied the same problem in more detail, using different numerical techniques and focused only on perfectly conducting partitions. They have reported that perfectly conducting partition increased the heat transfer due to fin's enhanced heating of the baffle, while the baffles disturbing the flow patterns had a decreasing effect. Also Xi and khodadadi proposed correlations of Nusselt number with regards to parameters studied for the specific case of perfectly conducting partitions. Later, Bilgen [19] numerically studied the same problem by considering strip to air conductivity values ranging from 0 to 60. For a completely adiabatic partition, he reported that at low Rayleigh numbers, a strip located close to the center yields maximum decrease in average Nusselt number. Moreover he reported that longer conductive partitions have a more remarkable effect on the flow field and heat transfer inside the cavity.

Oosthuizen and Paul [20] studied natural convection in rectangular cavities with aspect ratios between 3 to 7, with a horizontal plate at the center of the cold wall. They reported an increase in heat transfer due to the presence of adiabatic or perfectly conducting partitions on the cold wall. The effect of placing an array of horizontal partitions on the hot or cold walls, has been investigated [21-25]. Scozia and Frederick [21] considered slender cavities of $A = 20$ and taller, with multiple inclined conducting strips on the cold wall and with longer strips yielding lower average Nusselt numbers. They also reported that as the inter fin aspect ratio was varied from 20 to 0.25 and therefore number of fins increases, specific locations for the strip resulted in maximum or minimum values of mean Nusselt number, at different Rayleigh numbers. Facas [22] numerically studied the effect of conducting baffles length and orientation, when fixed on the hot and cold walls of a narrow cavity with adiabatic horizontal walls, with adiabatic top and bottom walls. He studied implementing a single baffle as one of the limiting cases in his studies and reported existence of multicellular flow for a non-dimensional baffle length of 0.1, which breaks down into secondary circulations for the baffle length equal to 0.3 or greater, for the specific case of height to width ratio equal to 15. Terekhov and Terekhov [24] considered the case of multiple adiabatic or infinitely heat conducting horizontal partitions mounted on the hot wall of a cavity with adiabatic horizontal walls for an aspect ratio of 35. They found that for adiabatic strips, there is an optimum number which can yield the lowest average heat transfer.

Bilgen [26] studied natural convection in cavities with height to width ratios of 0.3 to 0.4, when one or two conductive partial partitions are placed at two different positions on the adiabatic horizontal walls. Nowak and Novak [27] examined natural convection heat transfer in slender rectangular cavities of aspect ratios higher than 15, equipped with two small vertical partitions, located in the middle of horizontal walls. They reported two small vertical partitions of the same length, made of glass and located in the mid-plane of the cavity may reduce mean Nusselt number by up to six percent. These works have carried out studies on vertical partitions with infinite or finite thermal conductivities. Oztuna [28] examined an enclosure with a conductive vertical partition fixed on the bottom wall, for $Ra = 10^4, 10^5, 10^6$. He reported as the partition's distance from hot wall increases, the average Nusselt number first decreases to a minimum and then increases for low Ra, while for high Ra, it first increases to a maximum and then decreases.

For cases with adiabatic partial partitions, Ciofalo et al. [29] have investigated the influence of various boundary conditions at the end walls and the partitions including adiabatic condition, when two symmetrical finitely thick partitions are extended from the center of upper and bottom walls for aspect ratios from 0.5 to 10. They have reported that the efficiency of partitions depends on Rayleigh number and aspect ratio, as well as partitions height in a complex way and is greatest for low Rayleigh numbers and high aspect ratios. Nansteel and Grief [30] performed an experimental study considering a partition suspended from the upper wall of a shallow cavity filled with water, for $Ra = 10^{10}$ to 10^{11}. Hanjalic et al. [11] studied the same turbulent problem numerically for Rayleigh number range of $10^{10} - 10^{12}$, and considered shallow cavities with an adiabatic partition at the center of the upper wall. Recently Ilis et al. [31] studied heat transfer reduction in square cavities, due to an adiabatic barrier fixed on the upper wall. They considered lengths up to one half of enclosure's height, and accounted for the effects of length and location of the partitions and reported that heat transfer reduction effectiveness depends on length and location of the adiabatic barrier and the Rayleigh number.

Our literature search has revealed that a comprehensive investigation of heat reduction capabilities of a single adiabatic horizontal partition, placed on either hot or cold wall has not been performed yet. Most of the previous studies have carried out studies on partitions with either infinite or finite thermal conductivities. Additionally, works on adiabatic partial partitions, have mostly either performed turbulent studies or have considered slender cavities of very high aspect ratio enclosures, in which some discussed applying a single adiabatic partition only as one of the limiting cases. They have not analyzed how increasing aspect ratio from $A = 1$ (square enclosure) to higher aspect ratio cases contributes to the evolution of multicellular flows, when horizontal partitions are used. Besides, effects of implementing a vertical partition in a higher aspect ratio enclosure, has not been considered in detail. Furthermore, comparisons between the effectiveness of horizontal and vertical partial partitions respectively mounted on the side or end walls for square and higher aspect ratio cavities needs to be studied.

In the present work we will study and compare vertical and horizontal adiabatic partial partitions in differentially heated rectangular cavities with insulated horizontal walls. The effects of length and location of the baffle will be taken into account for Rayleigh numbers from 10^3 to 10^6, with the main objective of determining how the parameters involved, could bring about maximum heat transfer depression across the system. The investigation is performed for square enclosures, as well as cavities with higher aspect ratios up to $A = 4$ and the computed data is correlated for all cases studied.

2. Problem definition and assumptions:

A schematic drawing of the enclosure, the two types of partitions under consideration, the boundary conditions and the coordinate system utilized in the present study is illustrated in Fig. 2.1. Height and width of the enclosure are respectively designated by *H* and *W*, and A is defined as the aspect ratio ($A = H / W$). The length of the geometry perpendicular to the plane of the figure is assumed to be long; therefore the problem is considered to be two dimensional. The enclosure is perfectly insulated on the top and bottom walls while there is a temperature gradient between the left and right walls which are respectively maintained at constant temperatures T_H and T_C, with $T_H > T_C$.

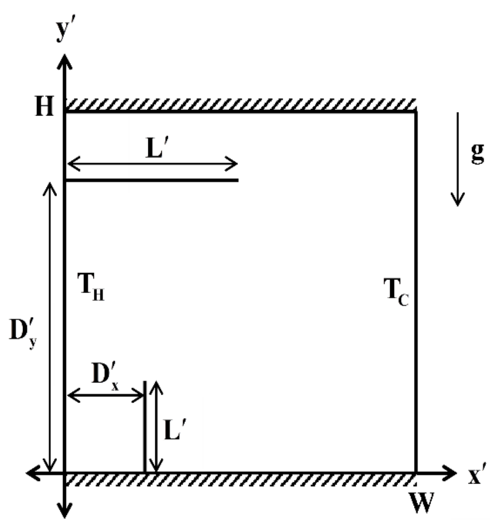

Figure 2.1 Schematic of the enclosure studied in the present work, along with representative vertical and a horizontal partial partition

A partition with length L' is fixed either on the sidewalls or on the top or bottom walls and is assumed to have negligible thickness and thermal conductivity. The dimensionless length of the partition is defined as $L = L' / H$ for vertical partitions and as

$L = L'/W$ for horizontal partitions. The distance from the hot wall to the vertical partition is designated as D'_x and the distance from the bottom wall to the horizontal partition as D'_y, which are referred to as the location of the partition. Dimensionless locations of vertical and horizontal partitions are defined as $D_x = D'_x/W$ and $D_y = D'_y/H$ respectively.

The working fluid in the domain is air which is considered to be Newtonian and incompressible, with $Pr = 0.71$. Gravitational body forces in negative y direction, act on the air present in the domain in which there are density gradients caused by the different temperatures of the sidewalls. The outcome is a buoyancy force which causes clock-wise circular convection currents of the fluid in the enclosure.

The air enclosed in the cavity is considered to have homogeneous thermophysical properties except for density, which is determined by the Boussinesq approximation. Rayleigh number varies from 10^3 to 10^6. In this range the flow is completely laminar and both conduction and free convetion contribute to the overall heat transfer of the system with convection playing progressively more important role as Ra increases. Heat transfer by radiation is considered to be insignificant and it is assumed that there is no viscous dissipation or thermal energy generation in the system.

3. Governing equations and boundary conditions:

Governing equations can be normalized by defining the following dimensionless parameters:

$$x \equiv \frac{x'}{W},\ y \equiv \frac{y'}{H},\ u \equiv \frac{u'W}{\alpha},\ v \equiv \frac{v'H}{\alpha},\ T \equiv \frac{T' - T_C}{T_H - T_C},\ p \equiv \frac{p'H^2}{\rho\alpha^2} \tag{2.1}$$

Parameters x and y are non-dimensional distances in the two perpendicular directions of the coordinate system. Variables u' and v' are local dimensional velocity components in the x and y directions; and T', p' are local values of temperature and pressure in the domain. Variables u, v, T and p are equivalent non-dimensional properties of the problem. In addition α is the thermal diffusivity coefficient and ρ is the density of the fluid. Based on the assumptions provided and the parameters introduced, dimensionless continuity, momentum and energy equations can be written as:

$$\frac{\partial u}{\partial x} + \frac{\partial v}{\partial y} = 0 \tag{2.2}$$

$$u\frac{\partial u}{\partial x} + v\frac{\partial u}{\partial y} = -\frac{\partial p}{\partial x} + Pr\left(\frac{\partial^2 u}{\partial x^2} + \frac{\partial^2 u}{\partial y^2}\right) \tag{2.3}$$

$$u\frac{\partial v}{\partial x} + v\frac{\partial v}{\partial y} = -\frac{\partial p}{\partial y} + RaPrT + Pr\left(\frac{\partial^2 v}{\partial x^2} + \frac{\partial^2 v}{\partial y^2}\right) \tag{2.4}$$

$$u\frac{\partial T}{\partial x} + v\frac{\partial T}{\partial y} = \frac{\partial^2 T}{\partial x^2} + \frac{\partial^2 T}{\partial y^2} \tag{2.5}$$

where $Pr \equiv \nu / \alpha$ and $Ra \equiv g\beta(T_H - T_C)W^3 / \alpha\nu$, β is coefficient of thermal expansion and ν is the momentum diffusivity of the working fluid. Boundary conditions are comprised of no slip conditions on all boundaries and the partition, along with isothermal conditions on the sidewalls and adiabatic conditions on the partition, and top and bottom walls.

$u = v = 0$ and $T = 1$ on the hot wall

$u = v = 0$ and $T = 0$ on the cold wall

$u = v = 0$ and $\partial T / \partial y = 0$ on the top and bottom walls (2.6)

$u = v = 0$, plus $\partial T / \partial y = 0$ on the horizontal partition

$u = v = 0$, plus $\partial T / \partial x = 0$ on the vertical partition

Nusselt number value at any point on the hot wall and the average Nusselt number over the hot wall can be calculated as:

$$Nu \equiv \frac{hL}{k} = -\left.\frac{\partial T}{\partial x}\right|_{x=0}, \quad \overline{Nu} \equiv \left.\int_{y=0}^{1} \frac{\partial T}{\partial x} dy\right|_{x=0} \tag{2.7}$$

where h, is the heat transfer coefficient and k is the thermal conductivity. $\overline{Nu}$ provides a measure of the total heat flux through the enclosure. When barriers are implemented, Nusselt number reduction ratio which represents the heat flux adjustments caused by the partitions is introduced as the ratio of $\overline{Nu}$ when the barrier is mounted, to the $\overline{Nu}$ in the absence of partitions:

$$R_r = \frac{\overline{Nu}_{\text{in the presence of partitions}}}{\overline{Nu}_{\text{in the absence of partitions}}} \tag{2.8}$$

By defining non-dimensional stream function as $\psi = \psi' / \alpha$, the normalized stream function values are calculated from:

$$u = \frac{\partial \psi}{\partial y}, \; v = -\frac{\partial \psi}{\partial x} \tag{2.9}$$

4. Numerical solution:

In the absence of partitions, velocity and temperature fields have a point reflection symmetry through the center point of the cavity, due to the geometry and the boundary conditions configuration of the problem. This symmetry can be visually inspected in Fig. 2.2a which presents streamlines and isotherms in the specific case of a square cavity filled with air, at $Ra = 10^6$. As such, only vertical and horizontal partitions, respectively fixed on the bottom and left wall are studied here, knowing that their reflected equivalents through the center point of the cavity, fixed on the other two walls yield similar results.

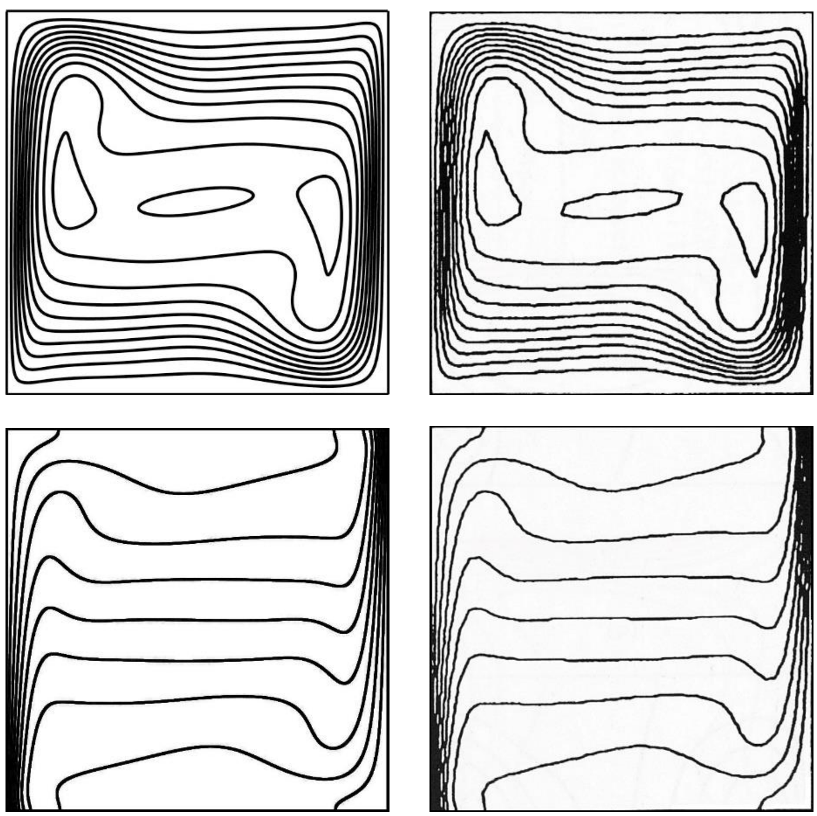

(a) (b)

Figure 2.2 Streamlines ($\psi: -16.27, \; -15.07(1.675)0$) and isotherms ($T: 0(0.1)1$) for $Ra = 10^6$ in the absence of partitions (a) present work, (b) results from de Vahl Davis [32]

A range of Rayleigh numbers from 10^3 to 10^6 are considered and the problem is solved for enclosures with four different aspect ratios, $A = 1, 2, 3, 4$ with a vertical or a horizontal partition mounted with three different values for the non-dimensional length, $L = 0.25, 0.5, 0.75$, and four different values for the non-dimensional location, $D_{x \text{ or } y} = 0.2, 0.4, 0.6, 0.8$. COMSOL Multiphysics software is used to solve the problem numerically, by means of finite element method. The PARDISO solver package in this program is set to directly solve the large sparse linear system of equations resulting from the governing partial differential equations (Eqs. (2.2)-(2.5)) in the discretized computational domain, with less than 10^{-4} relative error. The velocity and temperature fields are obtained and their contour profiles are plotted. Accordingly, the average Nusselt number ($\overline{Nu}$) on the hot wall and stream function values of the streamlines are calculated based on Eqs. (2.7) and (2.9), respectively.

4.1 Grid independence studies

The triangular mesh used in the present study has a non-uniformly distributed grid size, with a larger concentration on the walls and the partition compared to other regions. The distribution is controlled by manipulating four quantitative parameters which are the maximum and minimum allowed element size, the maximum rate at which the element size can grow and the curvature resolution, for which a lower value gives a finer mesh along the boundaries. Four different types of triangular mesh with different grid sizes have been generated with mesh type 1 being the coursest and mesh type 4 being the finest.

Specifications of each mesh type are presented in Table 2.1. By utilizing these four types of mesh, the computational domain for different cases studied in the prersent work are discretized to a number of triangular elements ranging roughly from 5×10^3 to 70×10^3.

Table 2.1 Grid independence study, specifying different mesh distributions that were experimented within this work. Numbers in parentheses are values at the boundaries and on the partition

Mesh type	Maximum element size	Minimum element size	Maximum element growth rate	Resolution of curvature
1	0.045 (0.0280)	0.02 (0.0040)	1.15 (1.1)	0.30 (0.25)
2	0.035 (0.0130)	0.01 (0.0015)	1.13 (1.08)	0.30 (0.25)
3	0.028 (0.0067)	0.004 (0.0002)	1.10 (1.05)	0.25 (0.20)
4	0.013 (0.0067)	0.0015 (0.0002)	1.08 (1.05)	0.25 (0.20)

At high Rayleigh numbers or when the partitions are mounted, finer mesh settings are required to achieve accurate results, due to increased complexity of the system. To confirm grid independence, a systematic set of computational runs were performed for all the cases studied. Due to wide variety of the situations being investigated, four different configurations of partial partitions in an air filled square enclosure with $Ra=10^6$ are chosen and presented here, as a sample of the grid independence studies performed. Case (I) is in the absence of partitions while cases (II) and (III) are when a thin vertical or horizontal partition with ($L=0.5$), fixed in the middle of the bottom or the left wall, respectively. In case (IV) a vertical partition ($L=0.25,\ D_x=0.5$) and a horizontal partition ($L=0.5,\ D_y=0.5$) are fixed in the square cavity simultaneously. Fig. 2.3 presents the grid independence study corresponding to the mesh types and the cases introduced. As can be seen, the differences between the $\overline{Nu}$ resulting from any pair of the mesh types 2,3 and 4 are always less than 1.5% for any of the four cases. This establishes very good accuracy for these three mesh sizes which are used in the present study compared to mesh 1 which is not used. Moreover, mesh 3 and 4 yield results less than 0.5% apart in any of four cases specified, and are used in most of the subsequent simulations.

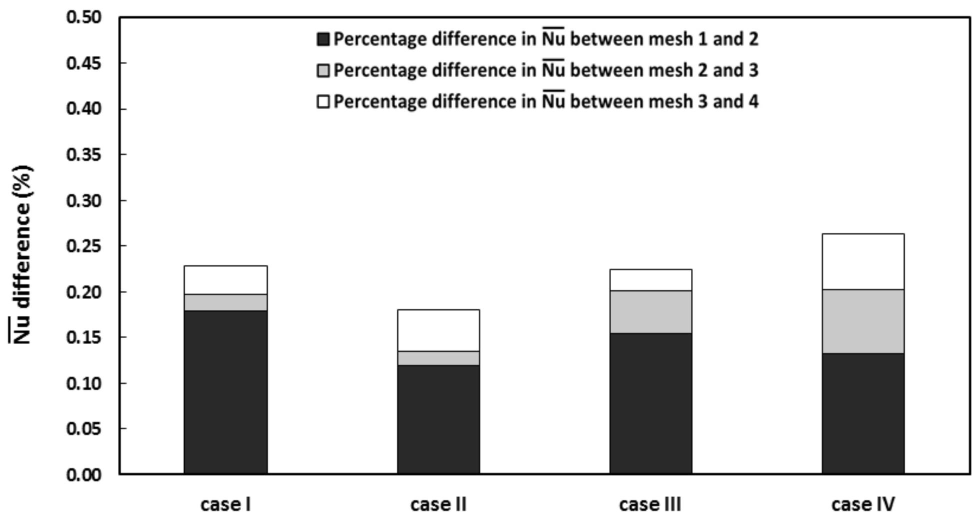

Figure 2.3 Effect of mesh concentration and grid independence study for $A=1$ and $Ra=10^6$. Case I) No partitions, Case II) a vertical partition with $L=0.5,\ D_x=0.5$, Case III) a horizontal partition with $L=0.5,\ D_y=0.5$, Case IV) a vertical partition with $L=0.25,\ D_x=0.5$ and a horizontal partition with $L=0.5,\ D_y=0.5$.

4.2 Effect of partitions thickness:

Partition's non- dimensional thickness is defined as $t=t'/W$, where t is the dimensional value of the thickness. In order to study the effect of t on the enclosure heat transfer, a vertical partition with $L=0.5$ and finite thickness is fixed at the middle of the bottom wall. Values of $\overline{Nu}$ and R_r corresponding to this configuration at $Ra=10^6$ are summarized in Table 2.2, for different t values.

Table 2.2 Effect of variations in the thickness of the partitions on $\overline{Nu}$ and Nusselt reduction ratios for $Ra = 10^6$ in the presence of a vertical partition($L = 0.5,\ D_x = 0.5$)

Thickness	$\overline{Nu}$	R_r	% **difference from t=0**
$t = 10^{-4}$	7.1786	0.8151	0.0032
$t = 10^{-3}$	7.1756	0.8148	0.0455
$t = 10^{-2}$	7.1295	0.8096	0.6866
$t = 2\times10^{-2}$	7.0968	0.8058	1.1421
$t = 5\times10^{-2}$	7.0028	0.7952	2.4515

Without any partitions the mean Nusselt would be $\overline{Nu} = 8.8067$, and when a partition is applied with zero thickness, $\overline{Nu} = 7.1788$. Table 2.2 shows that for thicknesses up to 2% of the width of the enclosure, results deviate less than 1.1% compared to the case when $t = 0$. Moreover real insulators have conductivities less than $0.1\, W/(m.K)$. Considering this value for the conductivity of the partition yields $\overline{Nu}$ values less than 0.15% apart for the case when $t = 2\times10^{-2}$ compared to when $t = 0$ and $k = 0$ .Hence, in the present work the thickness and conductivity of partitions are assumed to be zero, knowing that produced results are applicaple to situations with finite partition thicknesses and material conductivities, found in a real world setting.

5. Validation of the numerical model:

For validation purposes the computational results generated with our model are compared with the results available in the literature for an air filled square cavity differentially heated from the sides and insulated from the top and bottom. In Figs. 2.2 and 2.4 the streamlines and isotherms obtained in the absence of partial partitions are compared with the results from de Vahl Davis [32] and Barakos et al [33], at $Ra = 10^6$ as the most crirtical situation.

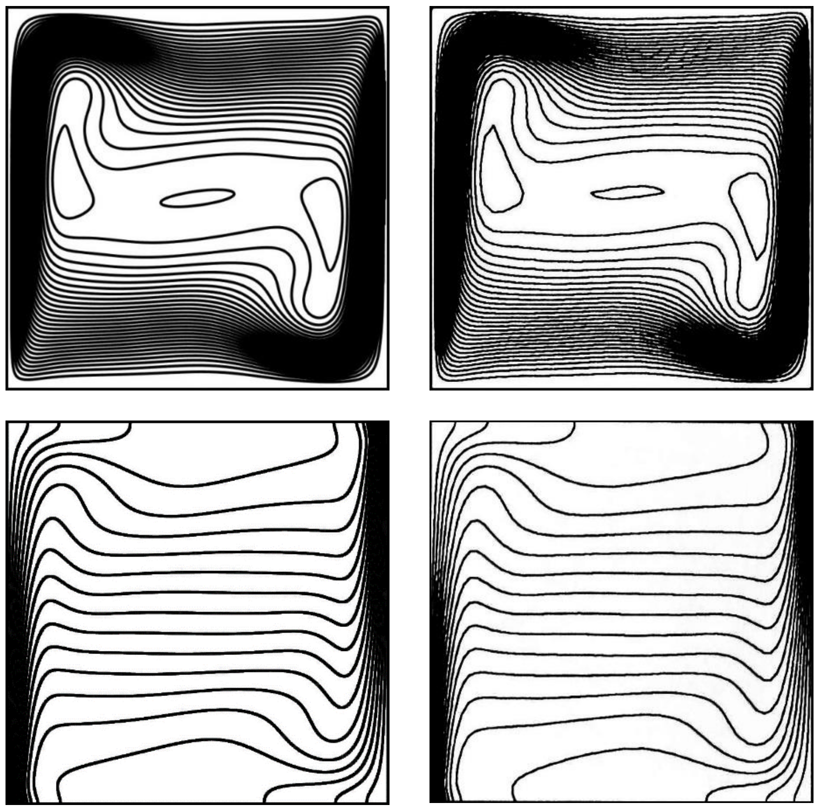

(a) **(b)**

Figure 2.4. Streamlines ($\psi : 0(0.605)16.335$) and isotherms ($T : 0(0.05)1$) for $Ra = 10^6$ in the absence of partitions (a) present work, (b) results from Barakos et al. [33]

In Table 2.3 mean Nusslet number values for $Ra = 10^3$ to 10^6, are compared with the works of various authors. The results from this study are always less than 0.1% apart from the results of de Vahl Davis [32]. Table 2.3 and Figs. 2.2 and 2.4, demonstrate excellent agreement between our results and previously published data.

Table 2.3 Comparison of mean Nusselt number ($\overline{Nu}$) with previous works for an enclosure with no partitions

Reference	$Ra = 10^3$	$Ra = 10^4$	$Ra = 10^5$	$Ra = 10^6$
Fusegi et al. [35]	1.105	2.302	4.646	9.012
Shi and Khodadadi [17]	-	2.247	4.532	8.893
Markatos and Pericleous [34]	1.108	2.201	4.430	8.754
Bilgen [19]	-	2.245	4.521	8.800
Nag et al.[16]	1.12	2.24	4.51	8.82
Ilis et al. [31]	1.11	2.24	4.51	8.80
Barakos et al. [33]	1.114	2.245	4.510	8.806
de Vahl Davis [32]	1.118	2.243	4.519	8.799
Present Work	1.118	2.244	4.519	8.807

Furthermore, when a partial partition is mounted in the enclosure, our model is validated through comparisons with limited numerically obtained results accessible in the literatre. In Fig. 2.5 an adiabatic partial partition with $L = 0.5$ is fixed on the top wall and at two different locations, and the generated streamlines and isotherms are compared with corresponding contour plots from Ilis et al. [31].

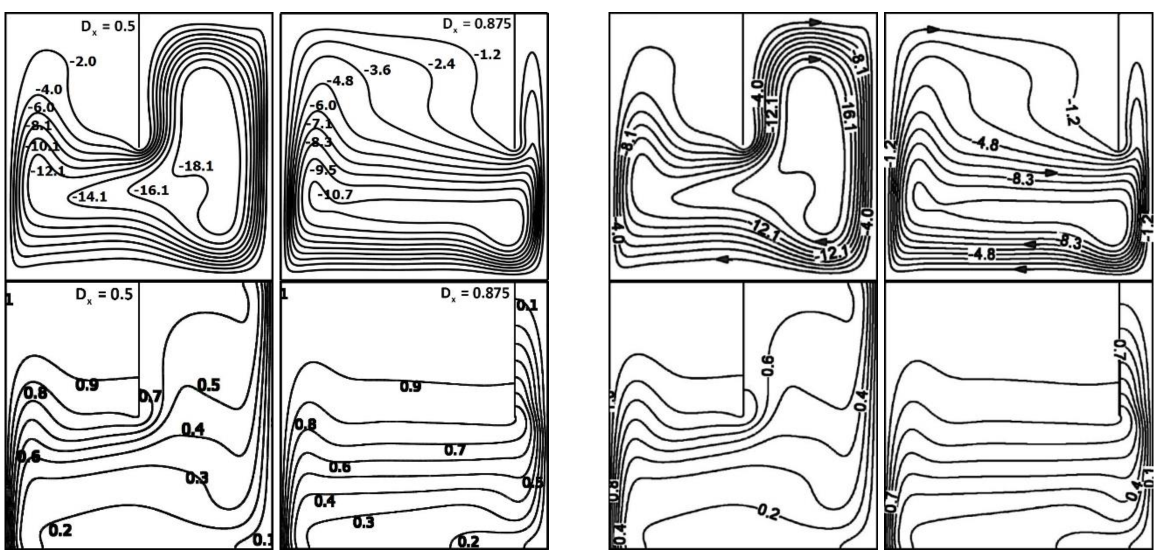

(a) (b)

Figure 2.5 Streamlines and isotherms for *Ra*=10^6 in the presence of a vertical partition fixed on the top wall (*L*=0.5, D_x=0.5, 0.875)) (a) present work, (b) results from Ilis et al. [31]

Also some $\overline{Nu}$ values are reported in Ilis et al. [31] for different configurations of a vertical partition fixed on the ceiling at various Rayleigh numbers which are compared with our result values in Table 2.4.

Table 2.4 Comparison of mean Nusselt number comparison with Ilis et al. [31] for an enclosure with a vertical partition mounted on the ceiling

Ra	L	D_x	R_r [31]	R_r present work	% difference
10^6	0.15	0.5	0.995	0.993	0.20
10^6	0.15	1.0	0.936	0.935	0.10
10^3	0.50	0.5	0.640	0.639	0.16
10^6	0.50	1.0	0.619	0.619	0.00
10^4	0.50	0.625	0.477	0.479	0.42
10^5	0.50	0.875	0.569	0.569	0.00

For any specific set, the results are very close and the difference is less than 0.5%. Additionally a diagram is presented in Ilis et al. [31] which depicts the variations of $\overline{Nu}$ reduction ratio with regards to the location of the vertical barrier on the ceiling and at various Rayleigh numbers, when $L = 0.5$. Same diagram is generated with our model and is presented in Fig. 2.6 along with the results from Ilis et al.

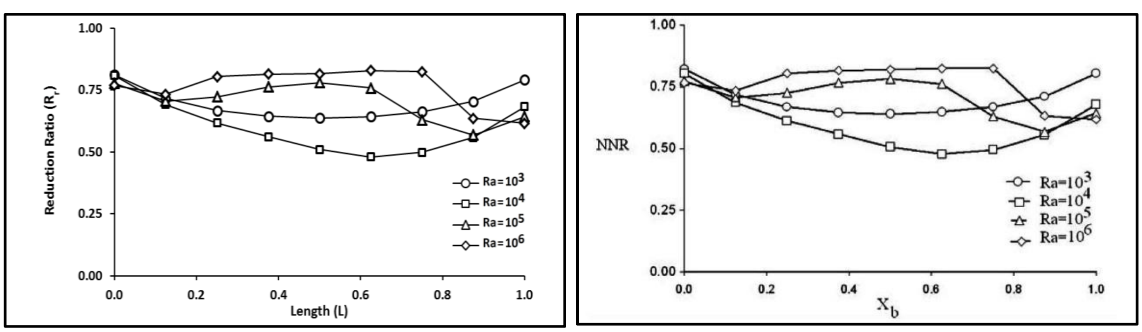

(a) (b)

Figure 2.6 Reduction ratio with respect to the location of the vertical barrier for L=0.5 at different Rayleigh numbers (a) present work, (b) corresponding results from Ilis et al. [31]

In Fig. 2.7a, a horizontal partition with $L = 0.7$ is mounted at the mid-height of the hotwall and it's conductivity is set to be equal to the conductivity of air, while Fig. 2.7b presents the contours produced by Bilgen [40], for the same setting. As can be seen in Figs. 2.5-2.7 and Table 2.4, a very good agreement exists between the results obtained by our model when a partition is mounted and the results reported in previously published works.

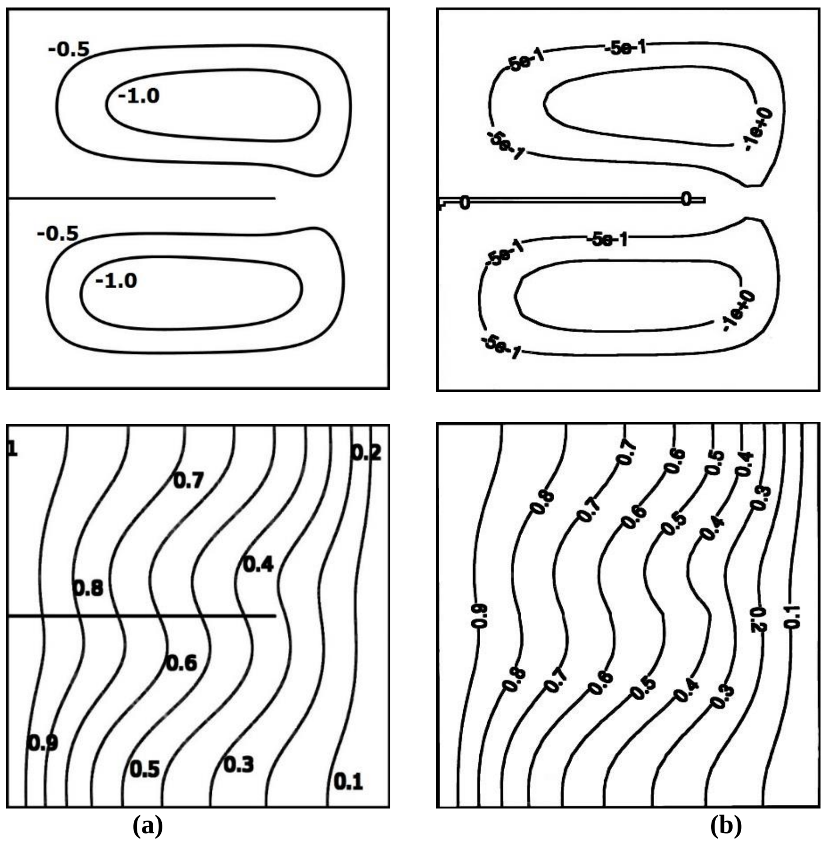

Figure 2.7 Streamlines and isotherms for Ra=10^4 in the presence of a horizontal partition fixed on the hot wall (L=0.7, D_y=0.5 and k_p=k_{air}) (a) present work, (b) results from Bilgen [19]

Since the top and bottom walls are insulated, the average Nusselt number on the hot wall, defined in Eq. (2.8) must equal to the same quantity on the cold wall. This was verified for all the cases studied in this work.

6. Results and discussion:

6.1 Vertical partition on the bottom wall:

When a vertical partition is attached, heat transfer is always smaller compared to an enclosure with no partitions, which leads to values of R_r smaller than one. Figure 2.8 demonstrates R_r variations with respect to Ra for $A=1$ to $A=4$ in an enclosure with a vertical partition fixed on the bottom wall. It can be seen in Figs. 2.8a-d that for any A, the non-dimensional length of the partition, L, has a significant effect on R_r, therefore the curves corresponding to similar lengths are grouped together. Implementing longer vertical adiabatic baffles reduces the convection heat transfer, by more effectively disturbing the flow, as well as blocking a larger portion of conduction.

In the case of a square enclosure (Fig. 2.8a) and at low Rayleigh numbers $(Ra=10^3)$, *1-D* conduction in the x direction is the dominant mode of heat transfer and the temperature gradient creates weak convection currents. When A and L are fixed and for $Ra=10^3$ changing the location of the partition would only disturb the minor buoyant flow and does not affect R_r considerably. But still, partitions located near the middle cause slightly lower R_r values. By increasing Ra convection plays an increasing important role in the overall heat transfer of the system. Consequently for fixed L, R_r gradually becomes more sensitive to D_x and also partitions block a larger portion of the overall heat transfer, leading to lower R_r minimums at 10^4.

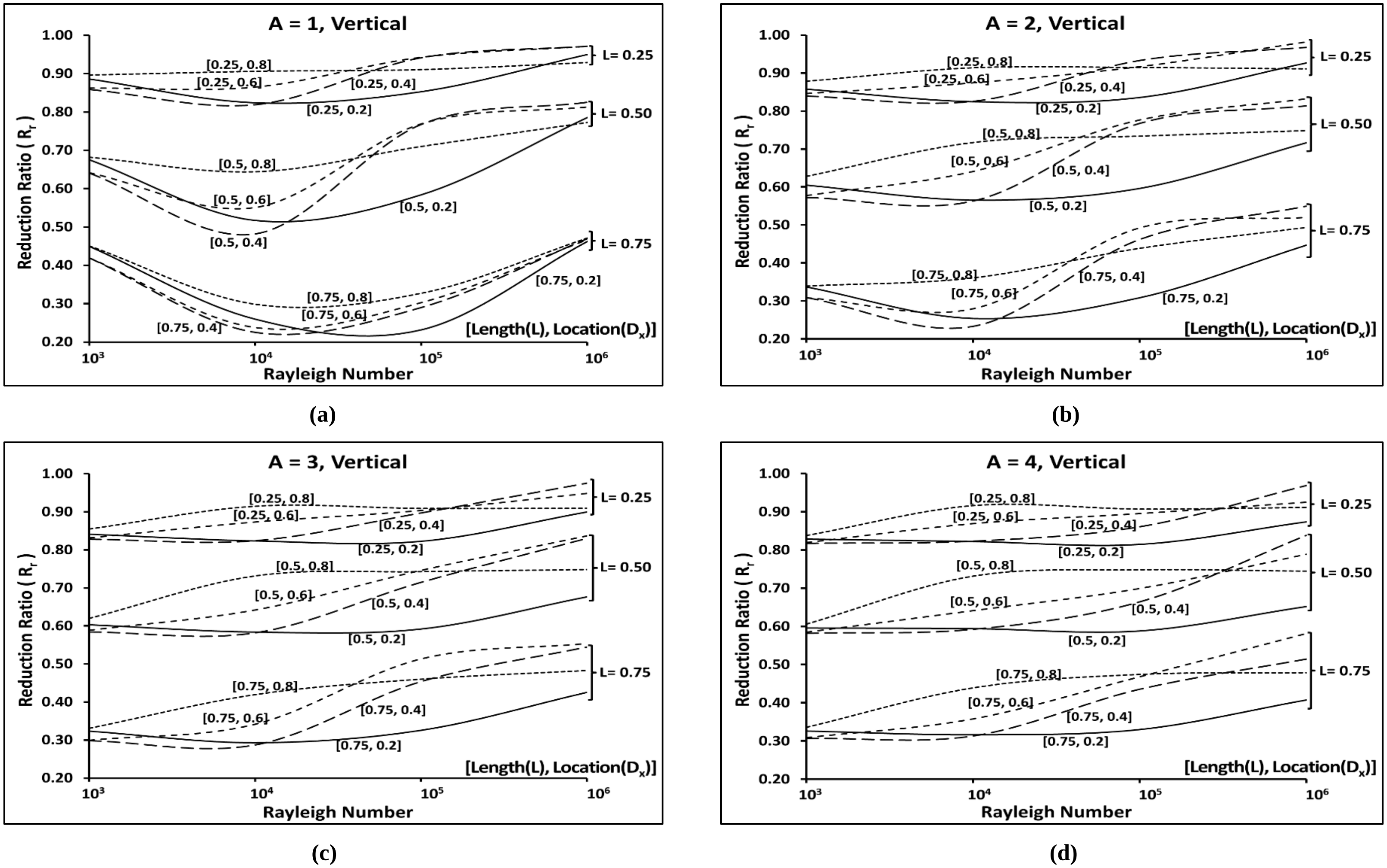

Figure 2.8 Reduction ratio variations with respect to Rayleigh number, length and location in the presence of a vertical partition for (a) A=1, (b) A=2, (c) A=3, (d) A=4

For a vertical partition of $L = 0.5$, minimum R_r occurs at $Ra = 10^4$ and $D_x = 0.4$, yielding an R_r as small as 0.48, which is considerably smaller than the minimums for the same setting at other Rayleigh numbers. Since length is the most significant factor, a partition with $L = 0.75$ could result in an R_r value as low as 0.21. Fig. 2.8a also reveals that by increasing Ra towards 10^6, generally R_r increases, indicating a decrease in partition's effectiveness, and also R_r becomes less sensitive to D_x. Additionally, partitions with $D_x = 0.8$ (near the cold wall) begin to produce lower reduction ratios compared to other locations. In all three groups, at $Ra = 10^3$, curves corresponding to $D_x = 0.4$ and $D_x = 0.6$ which have the same distance from the mid-plane, cross each other and yield the minimum R_r, indicating that the optimum position is close to the mid-plane. For $Ra = 10^3$ to 10^4, R_r minimum occurs around $D_x = 0.4$ and for higher Rayleigh numbers ($Ra = 10^4$ to $Ra = 10^6$) the minimum R_r occurs around $D_x = 0.2$. It can be concluded that by increasing the Rayleigh number, the D_x with minimum reduction is transferring from the center of the enclosure towards the hot wall.

Patterns associated with D_x in a square enclosure can be explained by considering the flow in an enclosure with no partitions. In the absence of obstacles and at low Rayleigh numbers the corners are relatively static regions due to the circular shape of the streamlines in the rectangular domain and an obstruction placed in these regions does not prominently redefine the flow. Instead streamlines are denser in the middle and as a result locations close to the mid-plane are optimum for heat transfer reduction.

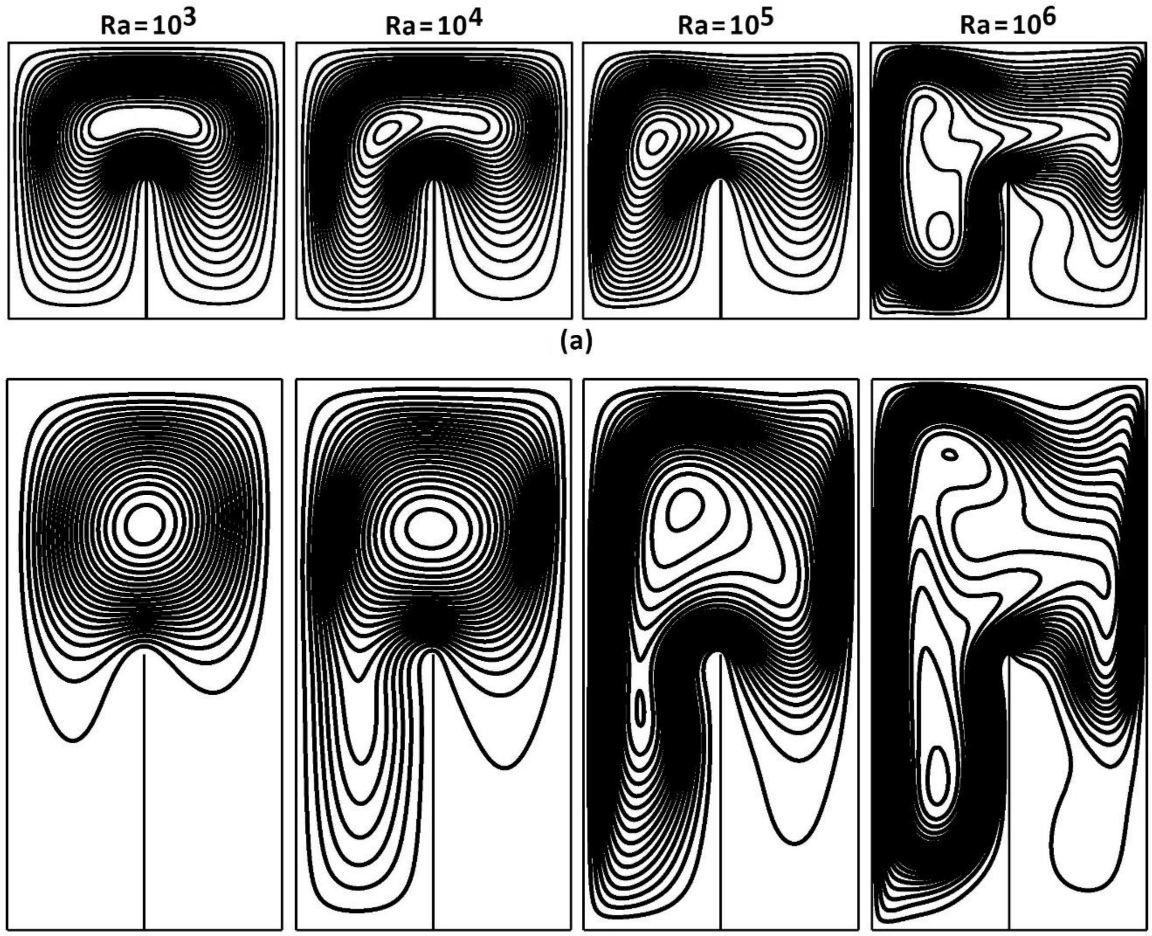

Figure 2.9 Streamlines at different Rayleigh numbers, when a partition with [L, D_x]=[0.5,0.5] is mounted, for (a) A=1 and (b) A=2

Figure 2.9a demonstrates the flow fields generated by attaching a partition with $L = 0.5$ in the mid-plane of the bottom wall at different Rayleigh numbers for $A = 1$. At $Ra = 10^3$, this figure illustrates how the vertical partition has affected the densely packed streamlines in the middle. By increasing Ra, this region of dense streamlines moves towards the hot wall and as can be seen in Fig. 2.2, at $Ra = 10^6$ streamlines become tightly packed close to the enclosure corners in the absence of partitions. Therefore the optimum D_x gradually decreases and a partition attached closer to the sidewalls disturb the flow more efficiently. Moreover, partitions close to the sidewalls also create relatively stationary regions between the partition and the sidewall, reducing the interaction between the fluid and the wall. This formation contributes to R_r reduction and is also mentioned by Ilis et al. [31].For these reasons locations close to the sidewalls are optimum at high Rayleigh numbers as high as 10^6. Fig. 2.9a also demonstrates that by increasing Ra towards 10^6 the flow becomes stronger and a thin boundary layer is formed. This thin boundary layer encompasses tightly packed streamlines (with relatively large stream function values) which curve around the obstacle. As a result the boundary layer interacts with the active sidewalls regardless of the value of D_x. This is the reason for the overall decrease in partition's effectiveness and the steady increase of R_r as Ra increases as seen in Fig. 2.8a.

In taller enclosures (Figs. 2.8b-d), the effect of partitions on the conduction is similar to the square cavity case. Again, partition's length remains dominant and increasing L considerably reduces R_r in all situations. While all other parameters are fixed, increasing A leads to a small reduction in R_r at $Ra = 10^3$. Specifically this decline is considerable when increasing the aspect ratio from $A = 1$ to $A = 2$ and for longer partitions ($L = 0.5, 0.75$); at $Ra = 10^3$ increasing the aspect ratio to $A = 2$ reduces R_r approximately by 8% for $L = 0.5$ and by 10% for $L = 0.75$. Conversely, Increasing A leads to a minor increase in R_r for $Ra = 10^4$ and 10^5. This increase in R_r is specifically considerable when shifting from $A = 1$ to $A = 2$, which is about $5 - 10\%$ for $L = 0.5$ at $Ra = 10^4$, and about $10 - 20\%$ increase for $L = 0.75$ at $Ra = 10^5$. Finally, changing A does not affect R_r at

$Ra = 10^6$. Because of these shifts, in Figs. 2.8b-d for fixed L and when the partition is fixed at the optimum location (D_x), R_r minimum values are almost equal for $10^3 < Ra < 10^5$. Therefore unlike when $A = 1$, the minimum R_r does not uniquely correspond to a specific Ra. For instance for $A = 3$ and $L = 0.5$, at $Ra = 10^3$, $D_x = 0.5$ leads to $R_{r,\min} = 0.57$; while at $Ra = 10^4$, $D_x = 0.4$ results in $R_{r,\min} = 0.58$ and at $Ra = 10^5$, $D_x = 0.2$ results in $R_{r,\min} = 0.59$ which are all apart only by 0.02.

Different characteristics of square and higher aspect ratio enclosures at low Rayleigh numbers can be explained by noting how increasing the aspect ratio influences the flow inside the cavity. In taller enclosures, partitions with similar non-dimensional lengths create narrower spaces between the partition and sidewalls compared to square enclosures. When Ra is small, it is harder for the flow to move in these narrower regions; therefore these relatively motionless areas start to play a more important role than in square cavities. At Ra numbers as low as 10^3, it is not possible for the flow to effectively penetrate into the narrow regions, which causes a large portion of the space surrounded in these regions to remain almost stationary with minimal heat interaction with the sidewalls. If the partition is located close to one of the side walls, only the space between the partition and that sidewall is almost stagnant. However when the partition is located close to the middle, the regions between the partition and both sidewalls become relatively motionless and this effect intensifies. Figure 2.9b demonstrates the flow fields generated by attaching a partition with $L = 0.5$ in the mid-plane of the bottom wall at different Rayleigh numbers for $A = 2$. Fig. 2.9b for $Ra = 10^3$ illustrates that only a single minimally disturbed circular flow emerges in the space over the partition which is actively contributing to the overall heat transfer in the system and the lower portion has minimal impact on heat transfer. Therefore the optimum position of the partition is in the mid-plane.

By gradually increasing Ra to 10^4 and 10^5 the streamlines tend to accumulate in a location left to the mid-plane, in absence of partitions. A partition located in these locations optimally pushes the circular stream upwards and yields minimum flow in both regions to the left and to the right of the partition. Consequently the optimum position shifts to locations to the left of the mid-plane, analogous to the square cavity case. Short partitions ($L = 0.25$) create gaps with considerably small height to width ratios, and this effect is almost insignificant. Therefore the curves corresponding to $L = 0.25$ are very similar in all four plots of Fig. 2.8. As can be expected longer partitions makes the effect of narrow regions more intense and the length's impact is significant similar to the case of square enclosures.

Figure 2.9 illustrates that as Ra increases towards 10^6, more vigorous currents are generated, with the potential to infiltrate in the narrow gaps and actively interact with sidewalls. As a result partition's effectiveness decreases and R_r gradually increases in all the curves of Figs. 2.8a-d. Moreover the effect of narrow regions becomes minimal and flow field's patterns become increasingly similar to the stretched version of the equivalent square setting; this can be observed by comparing Figs. 2.9a and 2.9b for $Ra = 10^6$. Consequently, as Ra increases towards 10^6, R_r values for $A > 1$ increase similar to the square cavity case. In the absence of partitions, at these high Rayleigh numbers, stronger boundary layer currents are tightly packed in the bottom corners, especially the left corner. Consequently fixing a partition close to the left wall (hot wall) disturbs the flow most effectively and yields minimum R_r. As such, partitions with $D_x = 0.8$ (near the cold wall) begin to produce lower R_r compared to locations close to the mid-plane. At $Ra = 10^6$, R_r is relatively more sensitive to D_x for $A > 1$ as compared to the $A = 1$ case, due to the narrow regions.

Figure 2.9 illustrates the disturbance of the main circulation pattern and its impact, at different Ra numbers. In the first row ($A = 1$), the partition is disturbing the flow by convoluting the streamline patterns, resulting in a heat transfer reduction at lower Rayleigh numbers. As Ra increases the stronger thin boundary layers become dominant. In the second row ($A = 2$) narrow regions are mainly responsible for the convection heat transfer reduction at lower Rayleigh numbers, and again the presence of a strong boundary layer attains dominance as the Rayleigh number increases. Similar patterns exist for a vertical partition attached on the upper wall, due to the symmetry considerations. For instance, in a square enclosure, increasing Ra would cause the location of the vertical partition on the ceiling with minimum R_r, to move from the center towards the cold wall. This is evident in Fig. 2.6 for the specific case of $L = 0.5$ and is also mentioned by Ilis et al. [31].

6.2 Horizontal partition on the hot wall:

Implementing a horizontal adiabatic partition on the vertical wall does not block conduction since its orientation is parallel to the conduction direction. Therefore these partitions essentially modify the convection portion of the overall heat transfer. Figures 2.10 and 2.11 demonstrate R_r variations with respect to Ra for $A=1$ to $A=4$ in an enclosure with an adiabatic horizontal partition mounted on the hot wall. Since the length is not the dominant parameter in this case, the results could not be grouped based on L in a single eloquent plot, similar to vertical partitions. Therefore for each aspect ratio the results are divided and presented in two plots. Plots on the left are for cases with the partition located close to top and bottom walls and plots on the right are for cases with the partition located close to the mid-height.

For Rayleigh numbers close to 10^3, the convection contributes to a small portion of the overall heat transfer. Consequently for horizontal partitions, when A is fixed and for $Ra=10^3$, changing the location or the length of the partition does not affect R_r significantly. Increasing Ra and implementing partitions with different L and D_y would produce an extended range of overall Nusselt reduction ratios.

In a square enclosure (Fig. 2.10a), implementing a horizontal partition leads to reduction in heat transfer ($R_r<1$). The decline in R_r is noticeable, though not as remarkable as a square cavity with a vertical partition. As expected, elongating the barrier makes it more efficient by more effectively disturbing the convective flow. This can be seen in Fig. 2.12a which demonstrates the flow fields generated by attaching a partition with different lengths in the mid-height of the hot wall cavity at $Ra=10^4$, for $A=1$. Nevertheless unlike the vertical partitions, L is not the main dominant parameter; instead, D_y also plays an important role.

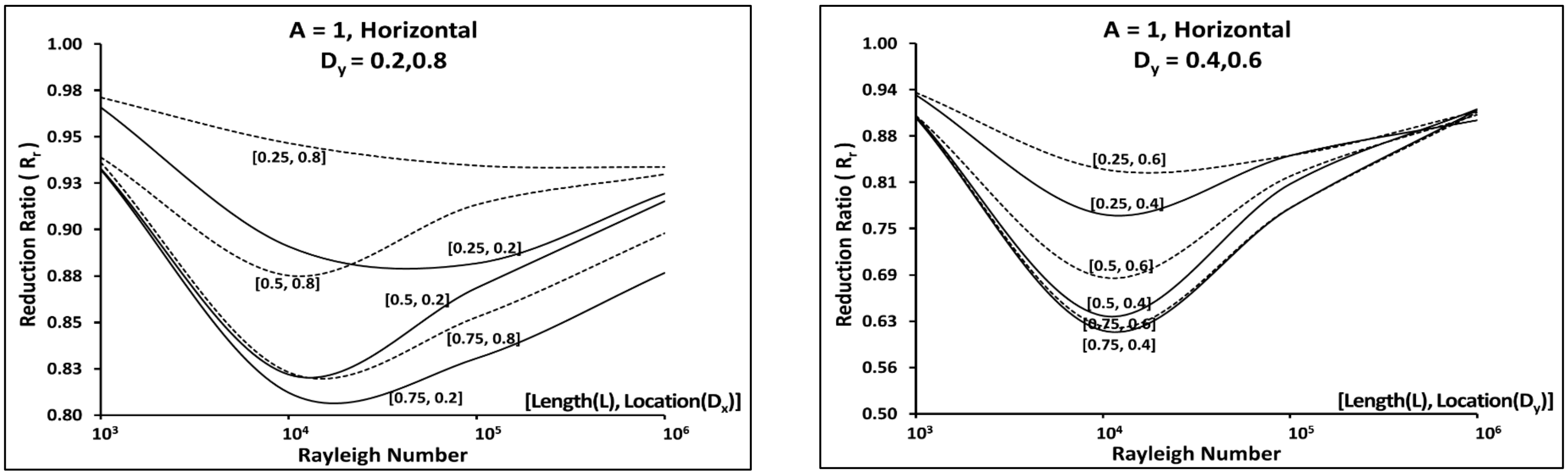

(a)

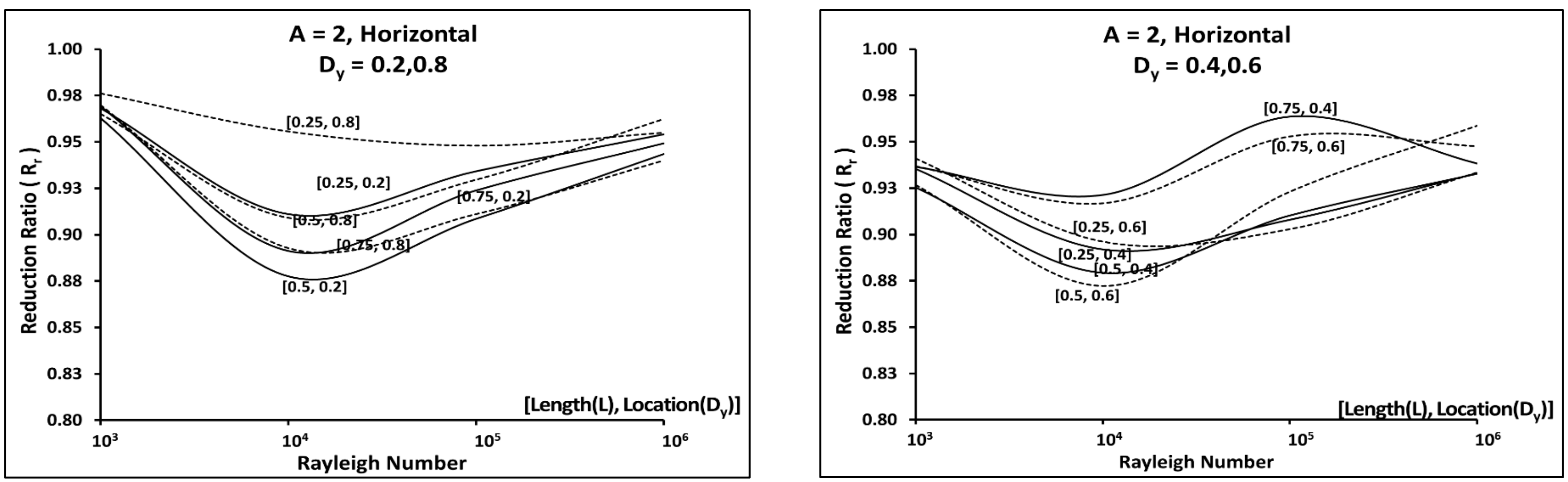

(b)

Figure 2.10 Reduction ratio variations with respect to Rayleigh number, length and location in the presence of a horizontal partition for D_y =0.2, 0.8 (plots on the left), and D_y =0.4, 0.6 (plots on the right) for (a) A=1, (b) A=2

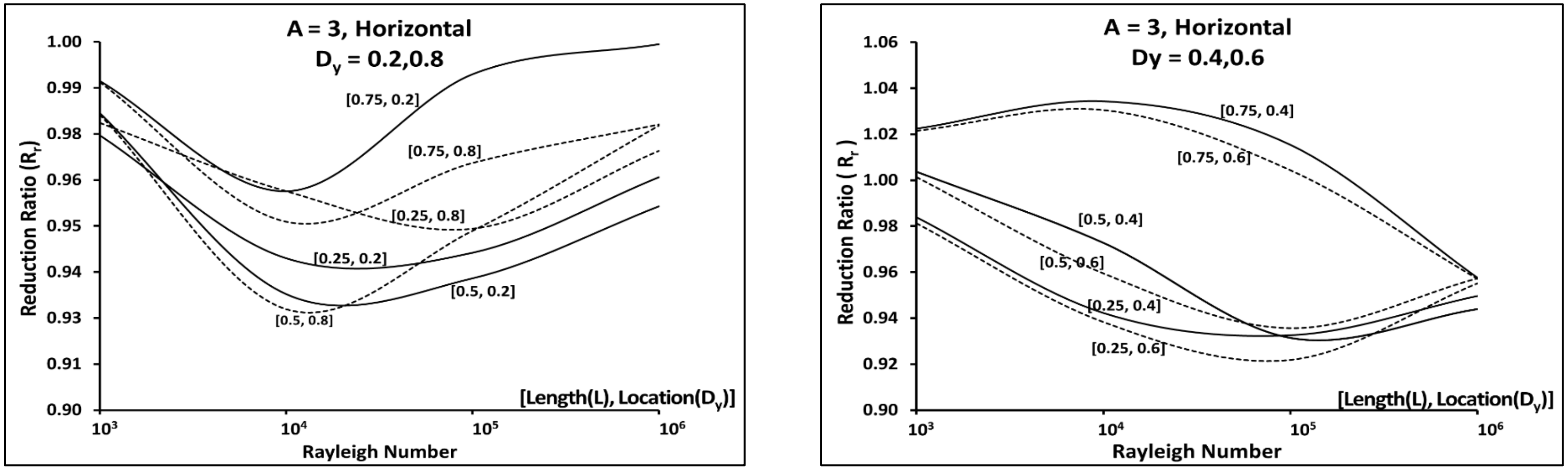

(a)

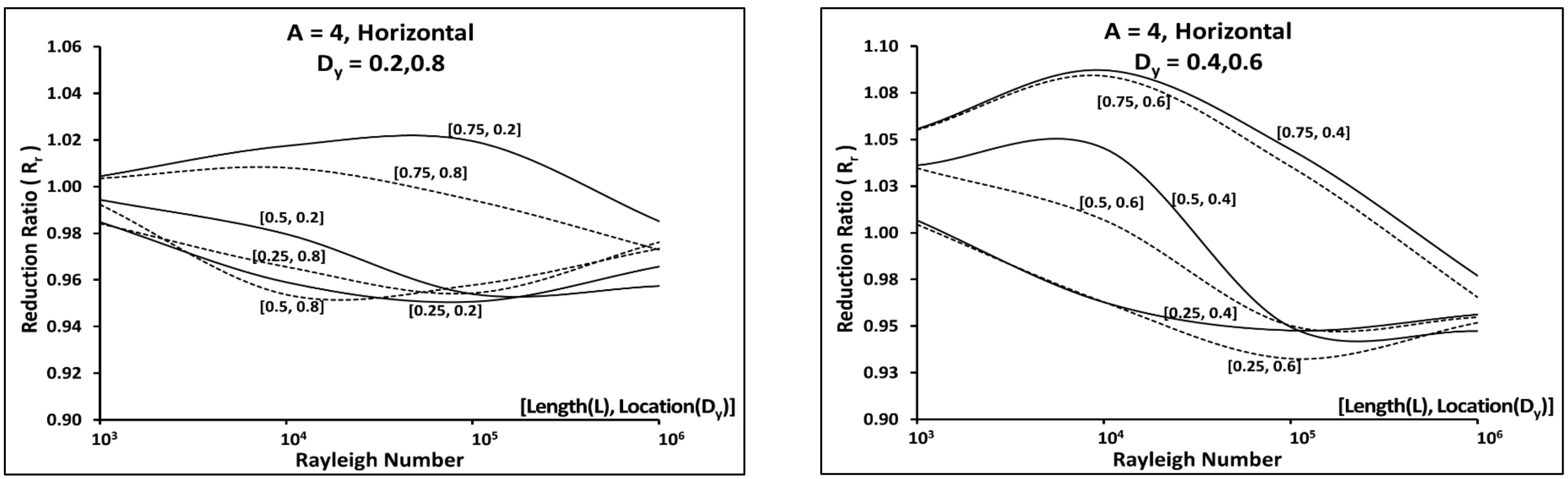

(b)

Figure 2.11 Reduction ratio variations with respect to Rayleigh number, length and location in the presence of a horizontal partition for D_y =0.2, 0.8 (plots on the left), and D_y =0.4, 0.6 (plots on the right) for (c) A=3, (d) A=4

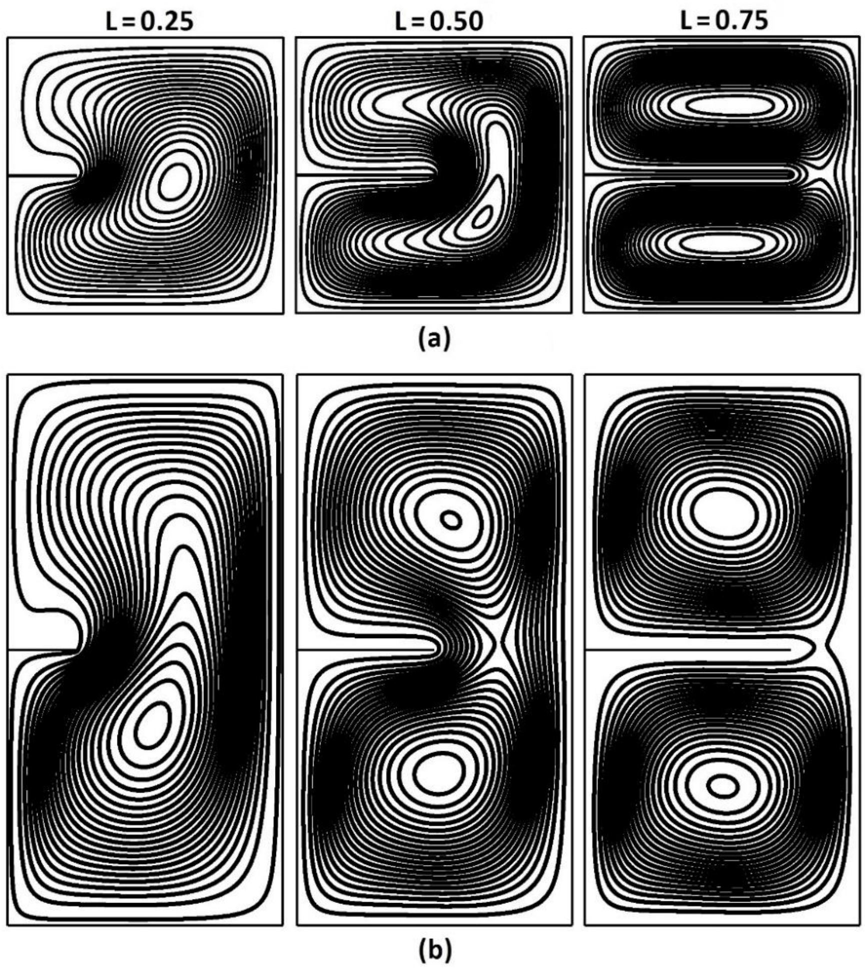

Figure 2.12 Streamlines at Ra=10^4 when a partition with D_x=0.5 and different Lengths is mounted, for (a) A=1 and (b) A=2

By comparing the two plots of Fig. 2.10a, it is clear that for $Ra > 10^3$, a horizontal partition located slightly below the mid-height ($D_y = 0.4$), is substantially more effective compared to a partition with the same length, located near the top and bottom walls. The reason is that as can be seen in Fig. 2.2 streamlines are more packed in this area in the absence of partitions, and a partition in this area most effectively disturbs the flow as it can be seen in Fig. 2.12. It is clear in Fig. 2.10a that the lowest R_r values occur around $Ra = 10^4$. Moreover unlike an enclosure with a vertical partition, changing Ra does not influence the relative effectiveness of partitions with different lengths and locations as much, and for all Ra values there is a specific set of $[L, D_y]$ leading to the minimum R_r. For instance for a partition within a square enclosure with $L = 0.5$, the optimum position is $D_y = 0.4$ for all Ra values, yielding an R_r as low as 63% at $Ra = 10^4$. Moreover, increasing Ra reduces the impact of both L and D_y, and around $Ra = 10^6$ they become somewhat insignificant resulting in a small range of R_r for a square cavity with a horizontal partition.

The aspect ratio has a universal influence on the average R_r of the system, and higher A produces higher R_r values. In taller enclosures ($A > 1$), with a horizontal partition, R_r is greater than 0.88, therefore reduction ratios are not as significant as the case of a square enclosure. Moreover for $A > 2$, some cases even yield R_r values bigger than one, which indicates that the partition has caused an increase in the overall heat transfer of the system. This makes the implementation of a single horizontal partition quite inefficient in tall enclosures. The reason is that for $A > 1$, horizontal partitions would partially divide the chamber into two smaller domains, leading to development of two relatively separate vortices between the hot and the cold wall. This triggers an increasing effect on the overall heat transfer of the system which opposes the R_r reduction caused by baffles manipulating the flow field. The formation of these duplicate circulations is clear in Fig. 2.12b which demonstrates the flow fields generated by attaching a partition with different lengths in the mid-height of the hot wall at $Ra = 10^4$, for $A = 2$. Comparing Figs.

2.12a and 2.12b shows that duplicate vortices are more prominent within taller cavities with horizontal partitions.

In Fig. 2.11, which correspond to cases that $A > 1$, R_r minimum occurs around Ra numbers between 10^4 and 10^5. As seen in Fig. 2.12b, longer partitions increase the probability of duplicate vortex formation. Therefore increasing length of the horizontal partition located close the mid-height can in fact augment the heat transfer after a certain point. As a result a partition with the same or higher length near the top or bottom wall can have an equivalent effectiveness. For instance, when $A = 2$ a partition with $[L, D_y] = [0.5, 0.6]$ or $[0.5, 0.4]$ would generate the minimum R_r at $Ra = 10^4$, equal to 0.87 or 0.88, respectively. A partition with the same length located close to the bottom ($D_y = 0.2$), would generate the same result ($R_r = 0.88$) at the same Rayleigh number. As such, for $A > 1$ the minimum R_r can be achieved by means of two options: First, implementing a baffle near the mid-plane where the vertical streamlines are dense, in order to disturb the flow, and at the same time implementing a partition short enough to avoid double vortex formation. As A increases, the maximum effective L corresponding to this option reduces, and D_y yielding minimum R_r gradually shifts from 0.4 to 0.6. Also, mounting a partition with the same or greater length near the top or bottom walls can take advantage of a larger interacting surface area without producing the double vortex formation. As Ra increases the optimum D_y corresponding to this option gradually shifts from 0.2 to 0.8. Based on our results, neither of these options is more effective than the other nor causes significant heat flux reduction.

For longer horizontal partitions located close to the middle of the chamber both vortices are fully developed. This can be seen for $L = 0.75$, in Fig. 2.12b at $Ra = 10^4$. Accordingly R_r values can become larger than one, as can be observed for some cases in Fig. 2.11. For instance for $A = 4$, $L = 0.75$ and $D_y = 0.4, 0.6$ results in an R_r which can be as high as 1.09, at $Ra = 10^4$. Similar analysis and conclusions could be drawn for a partition implemented on the cold wall, due to symmetry.

Based on our results, horizontal partitions on the sidewalls do not reduce the heat transfer as effectively as the vertical partitions on the top or bottom walls, with the exception of a few situations. In a square cavity ($A = 1$) at higher Rayleigh numbers ($Ra = 10^4, 10^5, 10^6$), short adiabatic horizontal partitions ($L = 0.25$) located near the mid-height ($D_y = 0.4, 0.6$) are $5-10\%$ more effective than any vertical partition with the same non-dimensional (L) fixed at any location (D_x), at the same Ra, due to more effective disturbance of convective currents. Nevertheless at $Ra = 10^3$ only the vertical adiabatic baffles can block the dominant conduction heat transfer and are more effective. Moreover in square enclosures, longer vertical adiabatic partitions ($L = 0.5, 0.75$) with the optimum D_x value (which is decreasing as Ra increases), are more effective at any Ra compared to equivalent horizontal partitions due to more effectively blocking both conduction and convection. In general, in higher aspect ratio enclosures narrow regions increase the effectiveness of vertical partitions while double vortex formations decrease the effectiveness of horizontal baffles. Thus for any $A \geq 1$ and for any fixed Ra, a vertical partition with appropriate L and D_x would yield a lower R_r compared to a horizontal baffle with the same non-dimensional values of L and D_y.

6.3 Comprehensive Correlation:

By interpolating the data gathered and the plots presented, the mean Nusselt number reduction ratio, R_r, can be estimated for the set of the input variables in the intervals investigated in this work. A statistical data set is generated based on the results gathered from the 384 simulations, and correlated by JMP software. A correlation for the mean Nusselt number reduction ratio, R_r, is obtained which incorporates the effects of the pertinent parameters such as the aspect ratio (A), Rayleigh number (Ra), length (L) and location (D_x or D_y). This Correlation is given in Eq. (2.10).

$$\begin{aligned} R_r &= \alpha_0 + \alpha_1 A + \alpha_2 L + \alpha_3 D_i + \alpha_4 Ra \\ &\quad + \alpha_5 (A - 2.5)^2 + \alpha_6 (L - 5)^2 \\ &\quad + \alpha_7 (D_i - 5)^2 + \alpha_8 (Ra - 277750)^2 \end{aligned} \tag{2.10}$$

Table 2.5 Correlation coefficients for R_r in an enclosure with a vertical or a horizontal partition

Coefficient	Vertical	Horizontal
α_0	1.12515	0.80657
α_1	-6.4994×10^{-5}	4.0750×10^{-2}
α_2	-0.997501	1.3935×10^{-2}
α_3	0.109223	1.5518×10^{-2}
α_4	4.0349×10^{-7}	-1.0177×10^{-7}
α_5	-2.6166×10^{-3}	-1.1469×10^{-2}
α_6	-0.641952	0.193655
α_7	-0.201510	0.175580
α_8	-5.88625	2.34×10^{-13}
Average error	4.02 %	3.28 %

In the above correlation, the subscript i stands for either x or y and α_0 to α_8 are the correlation coefficients. The values of the coefficients and the average associated errors for each case are presented in Table 2.5. This correlation covers both horizontal as well as vertical partitions studied in this work. Figure 2.13 shows the actual mean Nusselt number reduction ratio versus that obtained from the correlation, Eq. (2.10), for vertical and horizontal partitions. As can be seen predicted and actual values match satisfactorily in most cases, which establishes good accuracy for the introduced correlation expression introduced. There are only four points with noticeable residuals at the bottom of Fig. 2.13b which correspond to cases with horizontal partitions of $L = 0.5, 0.75$ and $D_y = 0.4, 0.6$ at $Ra = 10^3$. For these cases more accurate values of R_r can be obtained by means of the plots presented earlier.

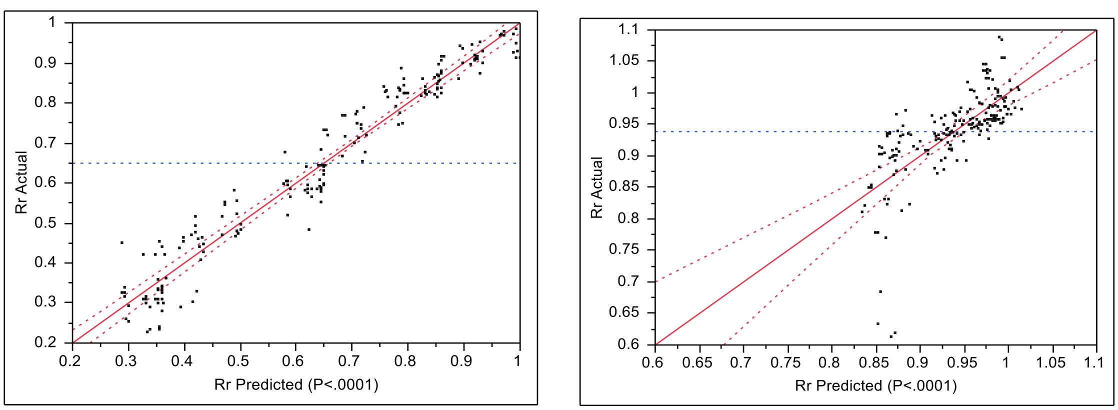

(a) **(b)**

Figure 2.13 Actual mean Nusselt number reduction ratio versus that obtained from the correlation Eq. (2.10) for (a) vertical partitions, (b) horizontal partitions

7. Conclusions:

Heat transfer reduction capability of a vertical or horizontal adiabatic partition fixed in a square or higher aspect ratio enclosures is studied, taking into account the effect of its length and location. Based on our results:

1. Vertical adiabatic partitions cause heat transfer suppression through the cavity while horizontal adiabatic partitions can increase the overall heat transfer, especially with higher values of length and in higher aspect ratio enclosures.
2. For vertical partitions, length is clearly the dominant factor, with longer partitions causing lower heat transfer rates, while for horizontal partitions both length and location play important roles, with regards to heat transfer reduction.

3 For vertical partitions in square cavities and for horizontal partitions in enclosures of different aspect ratios, first sensitivity of R_r to length and location augments, as Ra increases from 10^3 and then degrades as Ra further increases towards 10^6.

4. For heat reduction purposes, at Rayleigh numbers as small as 10^3 the optimum location for a vertical partition, is around the middle of upper or lower horizontal walls. As the Rayleigh number increases, regions close to sidewalls become progressively more favorable.
5. At low Rayleigh numbers, As the aspect ratios increases, vertical partitions more effectively reduce heat transfer due to formation of relatively motionless regions, and horizontal partitions become less effective (almost insignificant) due to increased potential for vortex formation. As Ra increases, the effectiveness of both vertical and

horizontal baffles becomes similar to their counterpart in square enclosures. The reason is formation of active cells within the regions separated by the baffles.

6. In general a partition can more effectively reduce heat transfer when it is vertically fixed on the top or bottom wall; except for a shorter horizontal partition, which can cause slightly more heat transfer reduction when located close to the mid-height of a square cavity as compared to an equivalent vertical case.

References:

[1] I. Catton, Natural Convection in Enclosures, Proc. 6th Int. Heat Transfer Conf., Toronto, Canada, vol. 6, pp. 13–43, 1978.

[2] S. Ostrach, Natural Convection in Enclosures, J. Heat Transfer, vol. 110, pp. 1175–1190, 1988.

[3] Y. Jaluria, Natural Convection Heat and Mass Transfer, Pergamon Press, Oxford, UK, pp. 209–235, 1980.

[4] E. M. Del Campo, M. Sen, and E. Ramos, Analysis of Laminar Convection in a Triangular Enclosure, Numer. Heat Transfer A, vol. 13, pp. 353–372, 1988.

[5] M. Corcione, Effects of the Thermal Boundary Conditions at the Sidewalls upon Natural Convection in Rectangular Enclosures Heated from Below and Cooled from Above, Int. J. Thermal Sci., vol. 42, pp. 199–208, 2003.

[6] A. Dalal and M. K. Das, Natural Convection in a Rectangular Cavity Heated from Below and Uniformly Cooled from the Top and Both Sides, Numer. Heat Transfer A, vol. 49, pp. 301–322, 2006.

[7] A. Bahlaoui, A. Raji, R. El Ayachi, M. Hasnaoui, M. Lamsaadi, and M. Naimi. Coupled Natural Convection and Radiation in a Horizontal Rectangular Enclosure Discretely Heated from Below, Numer. Heat Transfer A, vol. 52, pp. 1027–1042, 2007.

[8] R. L. Frederick, Heat transfer enhancement in cubical enclosures with vertical fins, Appl. Therm. Eng. vol. 27, pp. 1585–1592, 2007.

[9] Y. Varol, H.F. Öztop, F. Özgen, A. Koca, Experimental and numerical study on laminar natural convection in a cavity heated from bottom due to an inclined fin, Heat Mass Transfer, vol. 48, pp. 61-70, 2012.

[10] S. Jani, M. Mahmoodi, M. Amini, and J. E. Jam, Numerical investigation of natural convection heat transfer in a symmetrically cooled square cavity with a thin fin on its bottom wall, Therm. Sci., Issue 00, pp. 139-139, 2012.

[11] K. Hanjalic, S. Kenjeres, and F. Durst, Natural Convection in Partitioned TwoDimensional Enclosures at Higher Rayleigh Numbers,Int. J. Heat Mass Transfer, vol. 39, pp. 1407–1427, 1996.

[12] E. Zimmerman, and S. Acharya, Natural convection in an enclosure with a vertical baffle, Commun. Appl. Numer. M., vol. 4, pp. 631-638, 1988.

[13] R. L. Frederick and A. Valencia, Heat Transfer in a Square Cavity with a Conducting Partition on its Hot Wall, Int. Comm. Heat Mass Transfer, vol. 16, pp. 347–354, 1989.

[14] S. Acharya and R. Jetli, Heat Transfer due to Buoyancy in a Partially Divided Square Box, Int. J. Heat Mass Transfer, vol. 33, pp. 931–942, 1990.

[15] K. S. Chen, and P. W. Ko., Natural convection in a partially divided rectangular enclosure with an opening in the partition plate and isoflux side walls, Int. J. Heat Mass Transfer, vol. 34, pp. 237-246, 1991.

[16] A. Nag, A. Sarkar, and V. M. K. Sastri, Natural Convection in a Differentially Heated Square Cavity with a Horizontal Partition Plate on the Hot Wall, Comput. Meth. Appl. Mech. Eng., vol. 110, pp. 143–156, 1993.

[17] X. Shi and J. M. Khodadadi, Laminar Convection Heat Transfer in a Differentially Heated Square Cavity due to a Thin Fin on the Hot Wall, J. Heat Transfer, vol. 125, pp. 624–634, 2003.

[18] S. H. Tasnim and M. R. Collins, Numerical Analysis of Heat Transfer in a Square Cavity with a Baffle on the Hot Wall,Int. Comm. Heat Mass Transfer, vol. 31, pp. 639–650, 2004.

[19] E. Bilgen, Natural Convection in Cavities with a Thin Fin on the Hot Wall,Int. J. Heat Mass Transfer, vol. 48, pp. 3493–3505, 2005.

[20] P. Oosthuizen and J. T. Paul, Free Convection Heat Transfer in a Cavity Fitted with a Horizontal Plate on the Cold Wall, Advances in Enhanced Heat Transfer – 1985. Presented at the 23rd ASME National Heat Transfer Conference, vol. 43, pp. 101–107, 1985.

[21] R. Scozia and R. L. Frederick, Natural Convection in Slender Cavities with Multiple Fins Attached on an Active Wall, Numer. Heat Transfer A, vol. 20, pp. 127–158, 1991.

[22] G. N. Facas, Natural Convection in a Cavity with Fins Attached to Both Vertical Walls, J. Thermophys. Heat Transfer, vol. 7, pp. 555–560, 1993.

[23] R.L. Frederick, A. Valencia, Natural convection in central microcavities of vertical, finned enclosures of very high aspect ratios, Int. J. Heat Fluid flow, vol. 16, pp. 114-124, 1995.

[24] V. I. Terekhov, and V. V. Terekhov, Heat transfer in a high vertical enclosure with fins attached to one of the side walls, High Temp., vol. 44, pp. 436-441, 2006.

[25] V. I. Terekhov, and V. V. Terekhov, Heat transfer in a high vertical enclosure with multiple fins attached to the wall, J. Enhanced Heat Transfer, vol. 15, no. 4, pp. 303-312, 2008.

[26] E. Bilgen, Natural Convection in Enclosures with Partial Partitions, Renewable Energy, vol. 26, pp. 257–270, 2002.

[27] E.S. Nowak, M.H. Novak, Vertical partitions in slender rectangular cavities, Int. J. Heat Fluid Flow, vol. 15, no. 2, pp. 104-110, 1994.

[28] S. Oztuna, A Differential Quadrature Solution of Natural Convection in an Enclosure with a Partial Partition, Numer. Heat Transfer A, vol. 52, pp. 1009–1026, 2007

[29] M. Ciofalo and T. G. Karayiannis, Natural Convection Heat Transfer in a Partially—or Completely—Partitioned Vertical Rectangular Enclosure, Int. J. Heat Mass Transfer, vol. 34, pp. 167–179, 1991.

[30] M. W. Nansteel and R. Greif, Natural Convection in Undivided and Partially Divided Rectangular Enclosures, Journal of Heat Transfer, vol. 103, pp. 623]629, 1981.

[31] G. G. Ilis, M. Mobedi, H.F. Öztop, Heat Transfer Reduction due to a Ceiling-Mounted Barrier in an Enclosure with Natural Convection, Heat Transfer Eng., vol. 32, no. 5, 429-438, 2011.

[32] D. de Vahl Davis, Natural Convection of Air in a Square Cavity: A Bench Mark Solution, Int. J. Numer. Meth. Fluids, vol. 3, pp. 249-264, 1983.

[33] G. Barakos, E. Mitsoulis, and D. Assimacopoulos, Natural Convection Flow in a Square Cavity Revisited: Laminar and Turbulent Models with Wall Functions, Int. J. Numer. Meth. Fluids, vol. 18, pp. 695-719, 1994.

[34] N. C. Markatos and K. A. Pericleous, Laminar and Turbulent Natural Convection in an Enclosed Cavity, International Journal of Heat and Mass Transfer, vol. 27, pp. 755]772, 1984.

[35] T. Fusegi, J. M. Hyun, K. Kuwahara, and B. Farouk, A Numerical Study of ThreeDimensional Natural Convection in a Differentially Heated Cubical Enclosure, Int. J. Heat Mass Transfer, vol. 34, pp. 1543–1557, 1991.